Acta Pharmaceutica Sinica B 2025;15(11):5966−5987

Chinese Pharmaceutical Association
Institute of Materia Medica, Chinese Academy of Medical Sciences

Acta Pharmaceutica Sinica B

www.elsevier.com/locate/apsb
www.sciencedirect.com

ORIGINAL ARTICLE

Microneedle-facilitated *Portulaca oleracea* L.-derived nanovesicles ameliorate atopic dermatitis by modulating macrophage M1/M2 polarization and inhibiting NF-κB and STING signaling pathways

Meng Long[a,b,†], Jiaqi Li[a,b,†], Yuecheng Zhu[c], Hang Ruan[b], Jing Li[b], Fanjun Xu[b], Ruipeng Liu[b], Tao Yang[a,*], Yanqin Shi[c,*], Nianping Feng[a,b,*], Yongtai Zhang[a,b,*]

[a]*Center for Laboratory Animal Service & Experiments, the Seventh People's Hospital of Shanghai University of Traditional Chinese Medicine, Shanghai 200137, China*
[b]*School of Pharmacy, Shanghai University of Traditional Chinese Medicine, Shanghai 201203, China*
[c]*The Oriental Beauty Valley Group Metron (Shanghai) Technology Co., Ltd., the Oriental Beauty Valley Research Center for Active Plant Materials, Shanghai 201403, China*

Received 16 January 2025; received in revised form 23 March 2025; accepted 9 May 2025

KEY WORDS

Plant-derived nanovesicles;
Exosomes;
Microneedles;
Atopic dermatitis;
Portulaca oleracea L.;
Transdermal delivery;
Macrophage polarization;
Inflammation

Abstract Clinical management of atopic dermatitis (AD) is challenged by its susceptibility to recurrence, side effects, and high costs. We found that *Portulaca oleracea* L.-derived nanovesicles (PDNV) exert anti-inflammatory effects by modulating macrophage M1/M2 polarization. These effects were achieved through pathways including inhibition of nuclear factor-κB (NF-κB) and stimulator of interferon genes (STING) protein expression in diseased tissues, demonstrating their potential to ameliorate AD symptoms. To increase the transdermal permeation of PDNV, dissolvable microneedles composed primarily of hyaluronic acid (HA) were developed as an adjunctive means of delivery. Meanwhile, polysaccharides of *Portulaca oleracea* L., which were synergistic with PDNV, were used as microneedle constituent materials to enhance the mechanical properties and physical stability of HA. This new means of delivery significantly improves the treatment of AD and also provides new options for the efficient utilization of

*Corresponding authors.
E-mail addresses: dq2890@shutcm.edu.cn (Tao Yang), shiyanqin@obvmt.cn (Yanqin Shi), npfeng@shutcm.edu.cn (Nianping Feng), analysisdrug@126.com (Yongtai Zhang).
[†]These authors made equal contributions to this work.
Peer review under the responsibility of Chinese Pharmaceutical Association and Institute of Materia Medica, Chinese Academy of Medical Sciences.

https://doi.org/10.1016/j.apsb.2025.08.021

plant extracellular vesicles and the treatment of AD. In addition, transcriptomic analysis of PDNV showed that the mRNAs of *Portulaca oleracea* L. are closest to those of ferns, which may shed light on related evolutionary and plant species identification studies.

1. Introduction

Atopic dermatitis (AD) is a chronic and recurrent inflammatory dermatosis characterized by dry skin, intense itching, and eczema-like lesions that can affect individuals at any age and has a genetic predisposition[1-3]. Its main pathogenesis involves an imbalance in immune system signaling, genetics, skin dysfunction, and psychological factors[4]. Current treatments for AD, are mainly based on topical glucocorticosteroids, biologics, oral antihistamines, and ultraviolet light therapy[5,6], but have certain limitations, including serious adverse effects and unstable efficacy. Therefore, the search for safer and more effective treatment options has become a hotspot in dermatology.

With the increasing understanding of the pathomechanisms of AD, therapeutic strategies have gradually shifted from traditional symptomatic treatment to targeted therapy against the pathological process[7]. Among these strategies, plant-derived nanovesicles have shown potential in treating immune diseases, including AD. Nanovesicles derived from plant cells are encapsulated with active substances such as proteins and nucleic acids[8], which play vital roles in intercellular communication and immune regulation[9]. Although the discovery of plant-derived nanovesicles preceded that of animal-derived extracellular vesicles by about 15 years, plant-derived nanovesicles have been less studied[10]. In recent years, with the discovery of immunomodulatory and anti-inflammatory functions of some plant-derived nanoparticles, research in this area has rapidly heated up. For example, *Pueraria lobata*-derived nanovesicles have been reported to ameliorate cellular inflammation by downregulating pro-inflammatory gene expression and converting M1 macrophages into M2 phenotype[11]. It has also been demonstrated that microRNA-396e (miR-396e) in garlic-derived nanovesicles modulates the expression of 6-phosphofructo-2-kinase/fructose-2,6-bisphosphatase 3 (PFKFB3), affects the metabolic reprogramming of macrophages, and attenuates inflammation in adipose tissue of obese mice through interactions between macrophages and adipocytes[12]. In addition, nanovesicles from fruits have been shown to possess anti-inflammatory properties, such as apple-derived nanovesicles altering the production of extracellular matrix in dermal fibroblasts, which negatively affects the activity of Toll-like receptor 4 (TLR4), and consequently down-regulates the pro-inflammatory NF-κB pathway[13]. In another study, by fusing with extracellular vesicles excreted from gingival mesenchymal stem cells, grapefruit-derived nanovesicles encapsulated the anti-proliferative immunosuppressant CX5461 to reduce the secretion of inflammatory factors, attenuate Th17 cell activation, and promote the infiltration of regulatory Treg cells, which ultimately improves the imbalanced immune microenvironment, thereby treating AD[14].

Portulaca oleracea L., an ancient medicinal plant, and the juice of its fresh branches and leaves are commonly used externally for the treatment of AD in traditional Chinese medicine clinics[15]. Its extracts have also been developed into cosmetic raw materials with skin-desensitizing properties[16]. *Portulaca oleracea* L.-derived nanovesicles (PDNV) were found to effectively inhibit the expression of neutrophil-associated marker myeloperoxidase and pro-inflammatory cytokines, including tumor necrosis factor-α (TNF-α), interleukin-6 (IL-6), IL-12, and IL-1β, in an animal model of colitis, while promoting anti-inflammatory cytokine IL-10 secretion[17]. However, PDNV exhibit a size range of 50 to 1000 nm[18] in diameter with considerable variability. Owing to their intact vesicular architecture and relatively large size, these vesicles encounter significant challenges in effectively traversing the skin barrier, thereby impeding the manifestation of their therapeutic potential.

Microneedle technology, which enhances drug penetration by forming microchannels in the skin and offers the advantages of minimal invasiveness, painlessness, safety, and easy-to-use[19], has shown great potential for efficient transdermal drug delivery. The use of dissolvable microneedle patches have been reported to be effective in delivering glucocorticoids and genome editing technology based on clustered regularly interspaced short palindromic repeat-associated nuclease protein 9 (CRISPR-Cas9) for the treatment of inflammatory skin diseases[20]. Additionally, microneedle technology has been utilized to encapsulate exosomes and animal-derived extracellular vesicles to enable precise drug delivery. For example, a frozen microneedle delivered milk-derived exosomes encapsulated with *TNF-α* siRNA into rabbits through localized transdermal delivery at acupoints to effectively treat rheumatoid arthritis[21].

Among the various types of microneedles, dissolvable microneedles have garnered the most attention due to their high biosafety, accurate delivery dosage, easy-to-use, and good patient compliance. For patients who require frequent administration at the same position, compared to slow-degrading artificial polymers, which may accumulate locally and thus pose a potential health risk, hyaluronic acid (HA), a biopolymer naturally produced in human skin, is widely used in a large number of applications[22-25]. However, HA is highly hygroscopic, and therefore HA-based microneedles could lose the depth of skin entry and the amount of drug delivered due to rapid water absorption and softening during puncture into the skin. Adding plant polysaccharides with water solubility and fast local transit and absorption has proven effective in improving the mechanical properties of dissolvable microneedles[26-28]. Therefore, the addition of *Portulaca oleracea* L. polysaccharides (POP), which exhibited immunomodulatory, antimicrobial, and antioxidant effects[29], should greatly alleviate the disadvantages of microneedles made with HA alone.

In the current work, we designed dissolvable microneedles with HA and POP to integrate PDNV for the treatment of AD. The physical properties of the microneedles were fully evaluated. The mRNA composition of PDNV was determined, and their effects and underlying mechanisms related to the amelioration of AD symptoms were investigated, thus paving the path toward future clinical applications of PDNV.

2. Materials and methods

2.1. Materials

Fresh *Portulaca oleracea* L. was collected from Jieyang, Guangdong, China. Dexamethasone acetate ointment was purchased from China Resources Sanjiu Pharmaceutical Company (Shenzhen, China). Sodium hyaluronate (molecular weight 50 kDa) was ordered from Lushang Freda Pharmaceutical Co., Ltd. (Ji'nan, China). Bicinchoninic acid (BCA) kit (batch No. 20221011) and 3,3′-dioctadecyloxacarbocyanine perchlorate (DiO) were bought from Keygen Biotech Co., Ltd. (Nanjing, China). Rhodamine B (RhB) was purchased from Macklin Inc. (Shanghai, China). 2,4-Dinitrochlorobenzene (DNCB) was purchased from Jiuding Chemical Technology Company (Shanghai, China). Coomassie Brilliant Blue Rapid Staining Solution (batch No. 030723231023) came from Beyotime Biotechnology (Shanghai, China). Human TNF-α was bought from PeproTech, Thermo Fisher Scientific Inc. (Rocky Hill, NJ, USA). 4′,6-Diamidino-2-phenylindole (DAPI) staining solution and CCK-8 kit (batch No. MA0218-Jun-151) were ordered from Dalian Meilun Biological Co., Ltd. (Dalian, China). Mouse IgE ELISA kit (batch No. AF-02339M1), TNF-α ELISA kit (batch No. AF-02415M1), and INF-γ ELISA kit (batch No. AF-02465M1) came from Aifang Biotechnology Company (Hunan, China). CD86-FITC antibody (batch No. B411759), CD206-PE antibody (batch No. B403624), and mouse IL-4 ELISA kit (batch No. B360822) were ordered from Nanjing BoYan Biotechnology Company (Nanjing, China). NF-κB p65 antibody (batch No. A22331) and STING antibody (batch No. A21051) were bought from Company ABclonal, Inc. (Wuhan, China). p-NF-κB p65 antibody (batch No. CY6367) and CD86 primary antibody (batch No. CY5238) were purchased from Abways Technology Company (Shanghai, China). CD206 primary antibody (batch No. 60143-1-Ig) was purchased from Proteintech Group, Inc. (Chicago, IL, USA). Trizol was purchased from Thermo-InvitroGen Company (Waltham, MA, USA). RT reagent Kit (batch No. RR047A) and TB Green qPCR reagent Kit (batch No. RR420A) were bought from Takara Bio Company (Tokyo, Japan). Other reagents were from Sinopharm Chemical Reagent Company (Shanghai, China).

2.2. Animals and cell lines

Healthy male BALB/c mice of SPF grade, weighing 18−20 g, came from the Animal Experiment Center of Shanghai University of Traditional Chinese Medicine. All animal experiments were approved by the Laboratory Animal Ethics Committee of Shanghai University of Traditional Chinese Medicine (Approval No. PZSHUTCM2303080001).

HaCaT cells and RAW264.7 cells were purchased from the National Collection of Authenticated Cell Cultures (Shanghai, China) and the Center for Excellence in Molecular Cell Science (Shanghai, China), respectively.

2.3. Extraction and characterization of PDNV

PDNV were isolated from fresh *Portulaca oleracea* L. juice by differential centrifugation using Optima XE-90 ultra-high speed centrifuge (Beckman Coulter, Inc., Brea, CA, USA) and lyophilized for storage[30]. The zeta potential and particle size were determined at 25 °C with a Nanozs 90 device (Malvern Panalytical Ltd., Malvern, UK), and the number and distribution of nanoparticles were determined with a Nanosight NS 300 device (Malvern Panalytical Ltd., Malvern, UK).

Appearance and morphology: the samples were placed on a sample-bearing copper mesh (200 mesh), dried naturally, stained with 2% (*w*/*v*) phosphotungstic acid solution for 3 min, and consequently observed with a JEM-1400 transmission electron microscope (TEM) (JEOL Ltd., Tokyo, Japan).

Protein content and molecular weight distribution: The total protein content in PDNV was determined according to the operating instructions provided by the BCA kit manufacturer, and the protein content showed a linear relationship with the absorbance in the range of 0−10 μg (Supporting Information Fig. S1). The molecular weight distribution of the proteins was determined by sodium dodecyl sulfate-polyacrylamide gel electrophoresis (SDS-PAGE) through routine procedures including electrophoresis at 80 V for 3 h, and staining with Coomassie Brilliant Blue Rapid Staining Solution for 1 h. The gel was eluted with ultrapure water and imaged in an Amersham Image 600 Gel Imaging System (GE HealthCare Technologies Inc., Chicago, IL, USA).

Blood compatibility: healthy mouse blood was washed with saline several times, and erythrocytes were collected by centrifugation at 4 °C and 2465×*g* for 10 min, and diluted to 2% (*v*/*v*) with saline. Saline solution containing PDNV with different protein concentrations was mixed with an equal volume of the erythrocyte suspension, while saline and ultrapure water were used in the blank and negative control, respectively. Mixtures were all incubated at 37 °C for 2 h before centrifugation at 2465×*g*, and the absorbance at 541 nm was measured. The same method was used to determine the hemolysis rate of POP and HA. The hemolysis rate was determined according to Eq. (1)[31]:

$$\text{Hemolysis}\ (\%) = \frac{A_{\text{PDNV}} - A_{\text{Saline}}}{A_{\text{Water}} - A_{\text{Saline}}} \times 100 \quad (1)$$

Storage stability: PDNV aqueous solutions were stored at different temperatures while lyophilized PDNV was kept at room temperature, and the changes in particle size as well as protein content were measured at selected time points.

Transcriptomics sequencing: total RNA was extracted from PDNV according to the conventional process, and RNA quality was assessed using an Agilent 2100 Bioanalyzer (Agilent Technologies, Palo Alto, CA, USA). Samples that met the quality criteria were sequenced on the Illumina platform at Majorbio Co., Ltd (Shanghai, China). Each group included three biological replicates. The RNA sequencing data were analyzed using bioinformatics techniques, and the threshold for differential expression was set at a fold-change of at least 2 (indicating upregulation or downregulation)[32].

2.4. Preparation and characterization of POP

The remaining dregs after extraction of PDNV were dried at 60 °C, and 10-fold (*w*/*v*) of pure water containing 1.5% (*w*/*v*) cellulase and 2.0% (*w*/*v*) pectinase was added. The solution was then adjusted to pH 5.0 with 0.1 mol/L hydrochloric acid, and subjected to enzymatic treatment at 50 °C for 100 min[33]. Subsequently, by adding pure water, the solution was further incubated at 75 °C for 4 h, and centrifuged at 3220×*g* for 20 min. The supernatant was concentrated by rotary evaporation at 60 °C for 2 h, followed by the addition of Sevag reagent (chloroform: *n*-butanol = 4:1), to remove protein. With the addition of 4-fold volume of anhydrous ethanol, the solution was incubated at 4 °C for 24 h, and centrifuged at 3220×*g* for 10 min. The

precipitate was dialyzed by a dialysis bag with a molecular weight cut-off of 3500 Da, and freeze-dried to obtain the POP. The total soluble sugar content of POP was determined using a standard curve of D-glucose standard solution of different concentrations (Supporting Information Fig. S2).

The infrared absorption spectra of POP were determined by scanning in the range of 4000−300 cm^{-1} using an R330 infrared spectrometer (Thermo Fisher Scientific, Waltham, MA, USA). The monosaccharide constituents in POP were analyzed by acid-hydrolyzed ion chromatography[34] by a Thermo ICS 5000+ Ion Chromatography System (Thermo Fisher Scientific, Waltham, MA, USA) equipped with a Dionex™ CarboPac™ PA20 (150 mm × 3.0 mm, 10 μm) liquid chromatography column, which eluted at 30 °C (Supporting Information Table S1) with a flow of 0.5 mL/min, and an electrochemical detector. Monosaccharide standards were mixed and dissolved in ultrapure water (Supporting Information Table S2). With the addition of 2 mol/L TFA acid solution, POP samples were heated at 121 °C for 2 h, blown dry under nitrogen, washed with methanol, and dissolved in ultrapure water before testing. Data were analyzed by Chromeleon software.

The molecular weight of POP was estimated by high-performance gel permeation chromatography (HPGPC) on an Agilent 1100 high-performance liquid chromatography (HPLC) (Agilent, Santa Clara, CA, USA) system with a refractive index detector (RID), using a series-connected column of KS-804 and KS-802, ID 8 mm, and length 300 mm (Shodex Co., Tokyo, Japan). The calibration curve was established using different pullulans with known molecular weights (P-5, P-10, P-20, P-50, P-100, P-200, P-400, and P-800, Shodex Co.). The column temperature was kept at 40.0 ± 0.1 °C. Sodium chloride solution (0.2 mol/L) was used as the eluent, and the flow rate was kept at 0.8 mL/min. All samples were prepared as 2 mg/mL solutions, and a 20 μL aliquot was injected for each run.

2.5. Preparation and characterization of microneedles

POP-integrated microneedles loaded with PDNV (POP-MNs-PDNV) and without PDNV (POP-MNs) were prepared by vacuum casting method. POP and HA were dissolved in PDNV solution (protein concentration of 1.5 μg/μL), evenly cast in a microneedle mold, kept at −0.08 MPa for 15 min, dried at 37 °C, and finally demoulded. POP-MNs were prepared by dissolving POP and HA in ultrapure water in the same way. The prepared microneedles were characterized as follows:

Drug loading: microneedles were dissolved in ultrapure water, centrifuged at 150,000×*g* for 90 min, and the precipitate was resuspended in ultrapure water. Drug loadings were calculated as the mass concentration of protein content of PDNV in the microneedles, which were determined by the BCA method.

Rheology: samples were determined at 25 °C using an MCR101 rheometer (ANTON PAAR, Graz, Austria) with a shear rate of 0.01−1000 s^{-1}, and the graphs of the changes of shear stress and shear viscosity with the increase of shear rate were recorded.

Morphology: samples were dried at the critical point, sprayed with gold, and then viewed by a Quanta 250 FEG scanning electron microscopy (SEM) (FEI Company, Hillsboro, OR, USA).

Mechanical strength: the microneedles were placed on a TMS pro texturizer (Food Technology Corporation, Georgia, GA, USA) with the tip facing upwards, and a cylindrical probe with a diameter of 6 mm squeezed the microneedles at the speed of 30 mm/min until the amount of deformation reached 40%, with an initial triggering force of 0 N. A graph of the variation of the pressure with the displacement was plotted.

Hygroscopicity: the moisture absorptivity of microneedles were evaluated by weighing the microneedles at different time points under 25 °C and 75% relative humidity. The percentage of weight gain of the microneedles compared with the original weight represents their hygroscopicity.

Puncture performance: the PDNV and substrate in POP-MNs-PDNV were labeled with the lipophilic cell membrane dye DiO (E_x/E_m = 484 nm/501 nm) and the water-soluble dye RhB (E_x/E_m = 546 nm/568 nm), respectively. The microneedles were pierced into the isolated skin of mice for 1 min, and the distribution of the fluorescence in the skin was observed with a TCS SP8 confocal laser microscope (CLSM; Leica Microsystems Inc., Buffalo Grove, IL, USA).

Solubility: microneedles were pricked into the isolated skin of mice, and removed at different time points. The remaining microneedles were observed with an S40-DMil optical microscope (Leica, Wetzlar, Germany). In addition, the microneedles that were made with 1% (*w*/*w*) methylene blue-labeled substrate, were pricked into translucent simulated skin, which was formed by boiling and solidification of a mixture of 1% agar and 7% Konjac flour, and the dissolution of microneedles and the release of methylene blue were filmed by the microscope.

Evaluation of skin irritation: POP-MNs-PDNV were applied onto shaved skin at the same position on normal mice until complete dissolution once a day for 7 consecutive days, and the skin irritation was assessed at different time points. Twelve hours after the last administration, the mice were executed, and the skin at the administration position was clipped and processed for routine paraffin embedding, sectioning and hematoxylin & eosin (H&E) staining. Pathological changes in the skin were observed microscopically.

2.6. In vitro transdermal permeation

A modified Franz diffusion cell was used to evaluate *in vitro* transdermal permeation. Isolated mouse skin was fixed between the donor and the receptor cells of the RYJ-12B transdermal diffusion instrument (Huanghai Pharmaceutical Inspection Instrument Co., Ltd., Shanghai, China) with the stratum corneum facing the donor cells. POP-MNs-PDNV with DiO-labeled PDNV and the aqueous dispersion of the DiO-labeled PDNV were applied to the mouse skin, in which protein concentrations of PDNV were both 1.5 μg/μL. The receiving medium was PBS solution at 37 °C, and the numbers of fluorescent nanoparticles in the receiving solution samples were determined by Nanosight NS300 (Malvern Panalytical Ltd., Malvern, UK).

2.7. In vivo transdermal permeation

POP-MNs-PDNV that were composed of RhB-labeled substrate and DiO-labeled PDNV, were pricked into the shaved skin on the back of normal mice away from light, and the aqueous dispersion of DiO-labeled PDNV was used as a control group. The protein concentrations of PDNV were 1.5 μg/μL in both groups. Mice were humanely sacrificed at various time points, and the skin at the administration site was fixed in formalin for 2 h, embedded in optimal cutting temperature (OCT) compound, quick-frozen in liquid nitrogen, and cut longitudinally (10 μm in thickness) on an

A114009 cryosectioner (Leica, Germany). The distribution of fluorescence in the skin was checked under the Cytation5 Cellular Imaging Detection System (BioTek, VT, USA).

2.8. *In vitro assessment of anti-inflammatory effects of PDNV and POPs*

Cytotoxicity of PDNV and POP: HaCaT cells and RAW264.7 cells were inoculated in 96-well plates at 1×10^4 cells/well and incubated at 37 °C with 5% CO_2 for 24 h, respectively. Different protein concentrations of PDNV and POP with different mass concentrations were then added into the culture medium and incubated with HaCaT cells and RAW264.7 cells for another 24 h, respectively, followed by the addition of 10% CCK-8 solution and further incubation for 2.5 h. The optical density (OD) value at 450 nm was measured by a Spark 10M microplate reader (Tecan, Männedorf, Switzerland). Cell viability, which indicates cytotoxicity, was calculated according to Eq. (2):

$$\text{Cell viability}\ (\%) = \frac{\text{OD}_{\text{Sample}} - \text{OD}_{\text{Blank}}}{\text{OD}_{\text{Normal}} - \text{OD}_{\text{Blank}}} \times 100 \quad (2)$$

Cellular uptake: HaCaT cells and RAW264.7 cells were inoculated in 6-well plates, and cultured for 24 h before testing. The cells were incubated with or without DiO-labeled PDNV (of which protein concentration was 600 μg/mL) for different periods of time, before being fixed by 4% paraformaldehyde, co-stained by 10 μg/mL DAPI, and observed by Cytation5 Cell Imaging Detection System. (DAPI: E_x/E_m = 340 nm/488 nm, DiO: E_x/E_m = 484 nm/501 nm).

Effects on inflammation-induced epidermal cell proliferation: HaCaT cells were first assessed against different levels of TNF-α to find out the optimal inducing dosage for the test model. Subsequently, HaCaT cells were treated with this optimal concentration of TNF-α, with or without various concentrations of PDNV, POP, and PDNV + POP, respectively, for 24 h, before being tested for cell viability by CCK-8 assay kit in accordance with the instructions provided by the manufacturer.

Effects on lipopolysaccharide (LPS)-induced inflammatory response: the optimum concentration of LPS to induce inflammatory response was determined by treating RAW264.7 cells with various amounts of the inducer and monitoring the NO expression by Griess method[35]. After the application of differential concentrations of PDNV, POP, and PDNV + POP, the levels of NO, TNF-α and IL-6 release in the supernatant were measured using the Griess method and ELISA kits.

RAW264.7 cell polarization assay: RAW264.7 cells were seeded and cultured in 6-well plates for 24 h. The cells were given 1 μg/mL LPS to induce polarization and were administered with or without 0.1 mg/mL (protein content) PDNV, 0.5 mg/mL POP, or 0.1 mg/mL (protein content) PDNV+2 mg/mL POP for 24 h. Subsequently, cells were treated with CD86-FITC (0.01 μg/μL) and CD206-PE (0.005 μg/μL) antibodies at 4 °C away from light for 30 min, washed with PBS, and analyzed by FACSCanto flow cytometry (Becton, Dickinson and Company, Franklin Lake, NJ, USA).

2.9. *Transcriptomics sequencing of RAW264.7 cells*

RAW264.7 cells were cultured in 6-well plates for 24 h, then were exposed to 1 μg/mL LPS, with or without 0.1 mg/mL (protein content) PDNV, 0.5 mg/mL POP, or 0.1 mg/mL (protein content) PDNV+2 mg/mL POP for 24 h. Other information on transcriptomics sequencing is the same as in 2.3 PDNV transcriptome sequencing. Gene expressions were analyzed and compared among different groups.

2.10. *In vivo pharmacodynamic evaluation*

1-Chloro-2,4-dinitrochlorobenzene (DNCB) was dissolved in a mixture of acetone and olive oil (4:1, *v/v*) to prepare for 0.5% and 1% DNCB solutions. Thirty-six mice were evenly and freely grouped into normal group (Control), model group (Model), positive control (dexamethasone acetate ointment, Dex) group, POP-MNs-PDNV group, POP-MNs group (blank microneedle), and PDNV group (aqueous PDNV solution). One day before modeling, mice were shaved 2 cm × 2 cm on the back. Mice in all groups, except for those in the normal group, were treated uniformly with 0.5% DNCB solution on their backs every day between Days 1−4, and further sensitized by applying 1% DNCB solution once every 3 days on Days 5 and 7−19[36]. Meanwhile, starting from Day 8 and for 14 consecutive days, distilled water, 2.5 g/kg Dex, POP-MNs-PDNV (300 μg of protein content of PDNV), POP-MNs, PDNV (300 μg of protein content) were applied daily to the backs of mice in corresponding groups. From Day 7 of the experiment, the area of dermatitis and severity index (EASI) (Supporting Information Table S3) were used for severity scoring[37]. The day after the final sample administration (Day 22), venous blood was drawn to isolate serum from every mouse. Mice were then humanely executed, and the skin at the site of administration and viscera were rapidly collected. The barrier repair function of the damaged skin was evaluated by taking the dorsal lesion skin of mice on the last day of administration and measuring the transdermal water loss rate by using a Tewameter mobile instrument (Courage + Khazaka electronic GmbH, Germany). The spleen was weighted, and the spleen index was expressed as the percentage of spleen mass against body weight. The isolated skin and viscera were fixed in formalin, and then paraffin-embedded and sectioned (3 μm thick).

Subsequently, H&E staining, toluidine blue staining, immunohistochemistry (IHC), and Western blot (WB) analysis were performed according to routine procedures. In the IHC assay, CD86 and CD206 antibodies were diluted at a ratio of 1:500, while NF-κB p65, p-NF-κB p65, and STING antibodies were all diluted at a ratio of 1:100, respectively. For WB analysis, p-NF-κB p65 and STING antibodies were diluted at a ratio of 1:1250, and NF-κB p65 was diluted at 1:5000. All of the above treated histopathological sections were visualized by S40-DMil optical microscope (Leica, Wetzlar, Germany), and the bands of the target proteins were detected with Amersham Image 600 Gel Imaging System (GE HealthCare Technologies Inc., Chicago, IL, USA).

The mRNA expression of TNF-α, IL-4 and IFN-γ in skin tissues was analyzed by RT-PCR, in which RNA extraction and RT-PCR were performed as usual. Briefly, RNA was extracted with Trizol reagent, followed by determination of RNA concentration with NanoDrop 2000 (Thermo Fisher Scientific, Waltham, MA, USA) and reverse transcription with RT reagent kits. The primer sequences used are shown in Supporting Information Table S4.

IgE in serum and TNF-α, IL-4 and IFN-γ in skin tissues were further detected by ELISA kits, and a TBA-40FR automatic biochemical analyzer (Toshiba Corporation, Tokyo, Japan) was used to detect serum alanine aminotransferase (ALT), aspartate transaminase (AST), total bilirubin (TBIL), creatinine (CR), urea (UR), and total serum protein (TP).

2.11. Data analysis

All data are expressed as mean ± standard deviation (SD). Statistical analysis was performed using GraphPad Prism 9.3.0 (La Jolla, CA, USA). *t*-Test was used in two group comparisons, and one-way ANOVA was employed for the comparison among multiple groups, with a *P* value of less than 0.05 being considered as statistically significant.

3. Results and discussion

3.1. Characterization of basic physical and biological properties of PDNV

Fresh *Portulaca oleracea* L. was washed with water, cut into small pieces, and juiced in a juicer. A low-speed centrifugation step (1200×*g* for 20 min and 3000×*g* for 20 min) was used to remove plant fibers and large particles. Then a medium-speed centrifugation step (10,000×*g* for 1 h) was used to remove cell debris and intact organelles. Finally, a high-speed centrifugation step (150,000×*g*, 1.5 h) was performed to obtain PDNV (Fig. 1A).

PDNV showed a typical teacup shape (Fig. 1B), with an average particle size of 122.3 ± 3.4 nm (Fig. 1C). The zeta potential of PDNV was −1.6 ± 0.4 mV. The number of PDNV obtained was $3.76 \times 10^9 \pm 6.35 \times 10^8$ particles per gram of fresh *Portulaca oleracea* L. (Fig. 1D). The protein content in 10 mg of lyophilized PDNV was 1.54 ± 0.18 mg, with the molecular weight of the proteins mostly less than 95 kDa (Fig. 1E). The hemolysis rates were below 5% for PDNV concentrations of 5−100 μg/mL PDNV (Fig. 1F), indicating their good blood compatibility and biosafety[38]. In addition, to maintain the stability of the particle size and the protein content, lyophilization is recommended to store PDNV, compared to aqueous solution (Fig. 1G and H).

3.2. mRNA profile analysis suggests the involvement of PDNV in the regulation of metabolic processes and immune responses to diseases

In total 15,850 unigenes were identified through PDNV transcriptome sequencing, and were subjected to GO functional annotation (Supporting Information Fig. S3). As a result, 9655

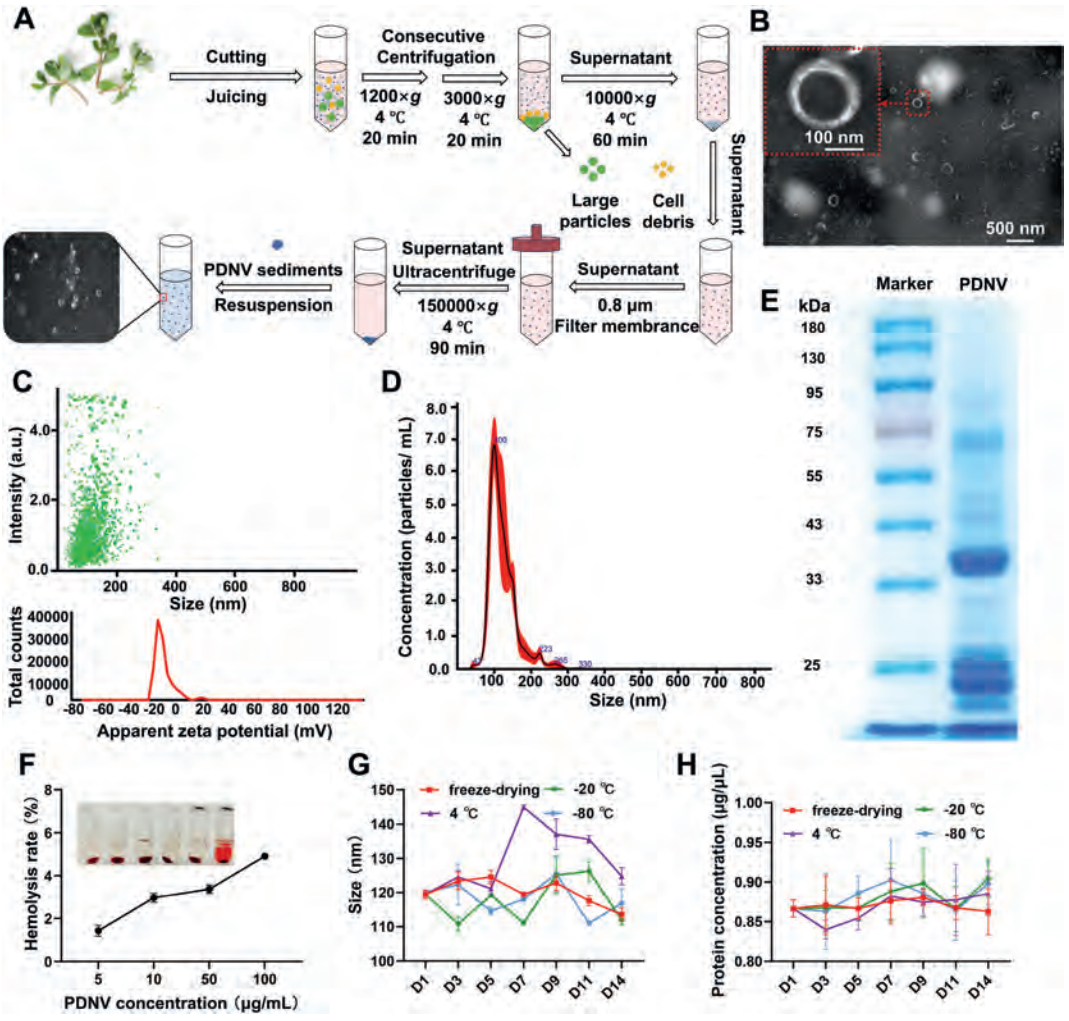

Figure 1 Extraction and characterization of PDNV. (A) Flowchart of PDNV extraction. (B) TEM image. (C) Particle size and zeta potential distribution of PDNV. (D) Particle number distribution of PDNV. (E) SDS-PAGE characterization of protein molecular weight distribution in PDNV. (F) Hemolysis rate of PDNV ($n = 3$). (G, H) Particle size and protein content analysis of PDNV in different storage conditions ($n = 3$).

(60.91%) unigenes were annotated, of which the three major categories of biological processes, cellular components and molecular functions accounted for the highest percentage. Then, KEGG pathway enrichment analysis was performed, and a total of 7103 (44.81%) unigenes were annotated (Supporting Information Fig. S4), of which the largest proportion was related to metabolic pathways connected to carbohydrate, amino acid, lipid and energy metabolism. Moreover, entries were found to enrich pathways relevant to genetic information processing and cellular processes. Taken together, enrichment of functions and signaling pathways analysis revealed that PDNV carry various active materials that are potentially significant to cellular function, metabolism, and processes.

EggNOG annotation resulted in 12,861 (81.14%) unigenes being annotated (Supporting Information Fig. S5), where the most annotated entries concentrated in posttranslational modifications, protein turnover, and chaperones, followed by signal transduction mechanisms, transcription, intracellular trafficking, secretion, and vesicular transport. NR annotation analysis was then performed, and 12,179 (76.84%) genes were able to annotate on the NR database (Fig. 2A). The percentage of gene species distribution was obtained from high to low as *Ceratopteris thalictroides* (L.) Brongn. (21.54%), *Adiantum capillus-veneris* L. (19.05%), and *Selaginella moellendorffii* Hieron. (15.55%), and ferns accounted for the majority of the genes, suggesting that *Portulaca oleracea* L. want to be close to ferns, which provides a reference for the identification and evolutionary studies of *Portulaca oleracea* L.

We continued to select the genes related to immunity from 15,850 unigenes by functional query and subsequently created a new gene set (12 genes), on which GO and KEGG functional

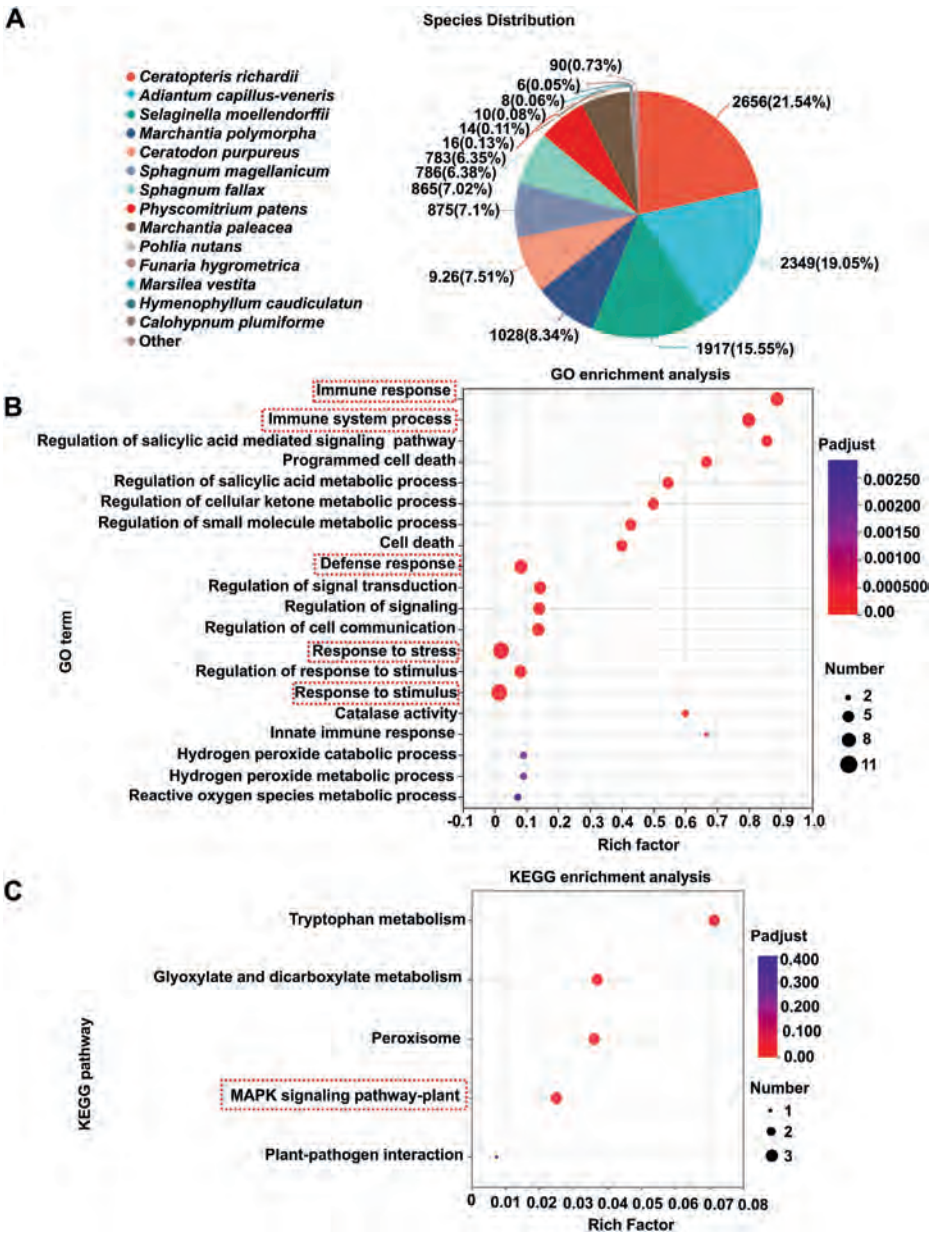

Figure 2 Transcriptomics data analysis of PDNV. (A) NR annotation graph. (B) GO enrichment graph. (C) KEGG enrichment map. (The red dashed boxes in the E and F highlight immune-related terms and signaling pathways).

enrichment analysis were performed. GO enrichment results (Fig. 2B) showed that the gene set was significantly enriched for entries on immune response (8 Go terms), defense response (11 Go terms), and stimulus response (11 Go terms). Meanwhile, KEGG enrichment analysis (Fig. 2C) revealed that the gene set was markedly enriched in five pathways, most of which were related to metabolic processes, but interestingly one of which is the mitogen-activated protein kinase (MAPK) signaling pathway. MAPK signaling pathway is an important intracellular signaling pathway involved in regulating a broad range of biological processes, including cell growth, differentiation, apoptosis, and response to stress. Aberrant activation of this signaling pathway has been associated with the development of a variety of abnormalities, including cancer, inflammatory diseases, and neurodegenerative diseases[39]. Taken together, we infer that PDNV may be involved in regulating metabolic processes as well as modulating certain diseases associated with immune responses.

3.3. POP-MNs-PDNV have superior physical properties

HA and POP were used as excipients for the dissolvable microneedles, and the hemolysis rates of both were less than 1% at concentrations up to 10 and 2 mg/mL (Supporting Information Fig. S6A and S6B), respectively, showing good blood compatibility. The infrared spectrogram of POP (Fig. 3A) showed a strong −OH stretching vibration peak near 3404 cm^{-1}, a C−H stretching vibration peak at 2938 cm^{-1}, a symmetric stretching vibration peak of C═O at 1744 cm^{-1}, an asymmetric stretching vibration peak of C═O at 1618 cm^{-1}, a distorted absorption peak of = CH_2 at 1411 cm^{-1}, a characteristic peak of protonated carboxyl group in uronic acid near 1411 cm^{-1}, a vibrational peak of unprotonated carboxyl group in uronic acid at 1244 cm^{-1}, and an absorption peak of C═O on the ring at 1111 cm^{-1}. The above results indicated that POP had the characteristic structure of polysaccharides[40]. The total soluble sugar content of POP was 60.67 ± 2%, and, as determined by the ion chromatograms of mixed monosaccharide standards and POP (Supporting Information Fig. S7A and S7B), the composition and molar ratio of each monosaccharide in POP were rhamnose: arabinose: galactose: glucose: galacturonic acid = 1.05: 2.62: 2.30: 1.91: 1.71, in which rhamnose, an L-deoxyhexose sugar, is found to be a functional unit in polysaccharides, which has antibacterial and anti-inflammatory effects[41]. The average molecular weight of the prepared POP was 111.11 kDa as determined by HPGPC (Supporting Information Fig. S8).

Microneedles were in the shape of a four-pronged cone, with a side length of 400 μm at the base, and a needle length of 800 μm (Fig. 3B). Microneedles were arranged in an 11 × 11 array, with a spacing of 1000 μm between the tips of the two neighboring needles (Fig. 3B). The microneedle morphology was intact, and the mold release rate was 100%. POP-MNs-PDNV were loaded with 2.23 ± 0.06 μg/mg of PDNV, but still had the same appearance and morphology as the POP-MNs (Fig. 3B), indicating that loading of PDNV did not affect the microneedle morphology.

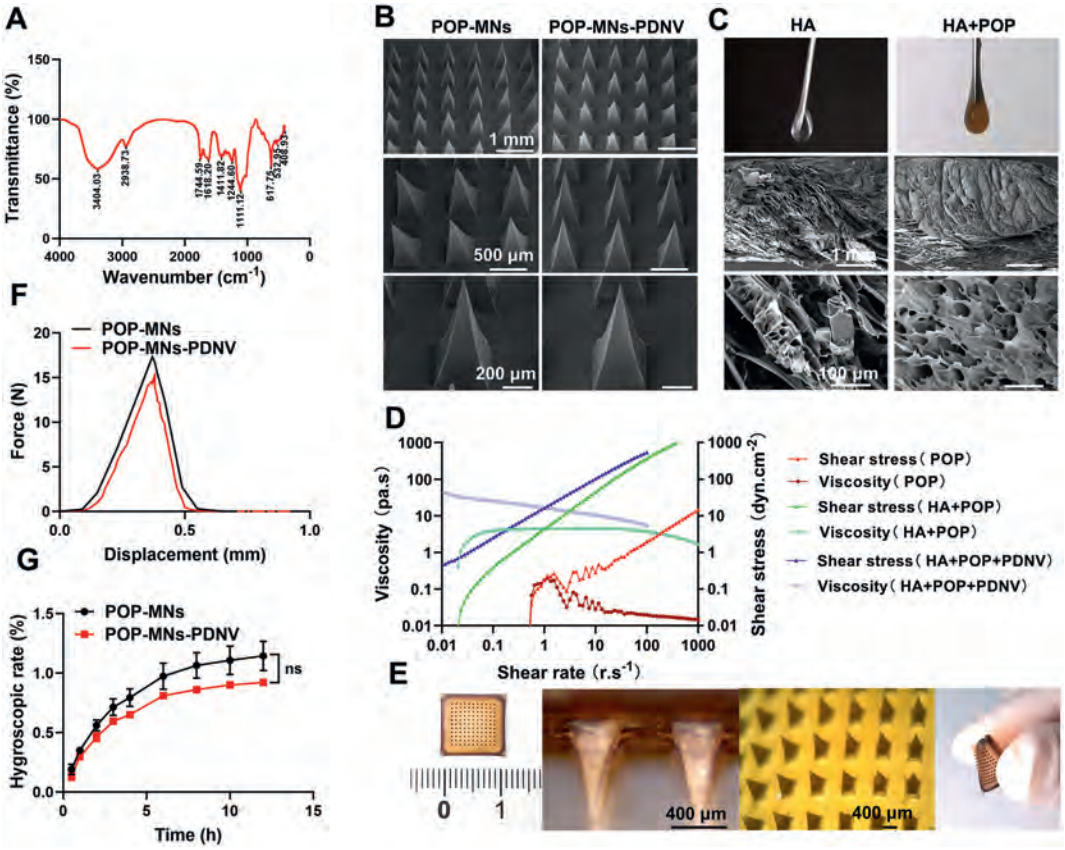

Figure 3 Characterization and properties of POP and microneedles. (A) IR spectra of POP. (B) SEM images of microneedles. (C) SEM pictures of internal structures of microneedle substrates. (D) Viscosity and shear stress variation against shear rate. (E) Appearance and measurements of the microneedles. (F) Force-displacement graph. (G) Plot of moisture absorption curve (n = 3).

The complete morphology and smooth surface of POP-MNs-PDNV were attributed to the excellent physical properties of the hydrogel substrate formed by HA and POP. The surface of the lyophilized HA hydrogel substrate was smooth and flat with a three-dimensional honeycomb network structure inside, while the surface of the POP-mixed substrate was slightly roughened with rounded pores inside but still maintained the three-dimensional honeycomb network structure, suggesting that POP did not disrupt the basic structure of the HA hydrogel (Fig. 3C). When the mixed substrate of HA and POP was in the hydrogel state, with the increase of shear rate, the shear stress increased, while the shear viscosity decreased, suggesting that the hydrogel was a non-Newtonian fluid, and had shear thinning performance and pseudoplastic fluid feature, which were conducive to vacuum injection into the mold to make microneedles. While aqueous POP solution with low concentration did not show the shear thinning property, which is characteristic of a Newtonian fluid and difficult to make by injection molding, its great viscosity may enhance the mechanical strength of HA (Fig. 3D). Indeed, bending the POP-MNs-PDNV patch, which was in the shape of a 1 cm × 1 cm square, can still maintain good form (Fig. 3E).

It has been previously reported that the hardness of microneedles generally needs to reach 0.004−0.16 N/needle in order to puncture the stratum corneum[42]. The mechanical strength of POP-MNs was 0.693 N/needle, and it was slightly reduced to 0.617 N/needle after the incorporation of PDNV (Fig. 3F), but still far beyond the minimum strength required to penetrate the cuticle. Furthermore, the addition of PDNV evidently reduced the hygroscopicity of POP-MNs, and it was worth noting that the maximum hygroscopic rates of both POP-MNs and POP-MNs-PDNV were less than 1.5% (Fig. 3G), which should be attributed to the physically modifying effect of POP on HA.

After puncturing into *ex vivo* mouse skin, both POP-MNs and POP-MNs-PDNV dissolved over half in 30 s and completely disintegrated in 3 min (Fig. 4A). Meanwhile, the microneedles fully dissolved in 1 min in artificial skin with higher water content, and incorporated methylene blue dye was slowly released in 5 min and completely diffused in 10 min (Fig. 4B). This rapid dissolution character of microneedles can shorten the administration time and improve patient compliance. With strong mechanical hardness, the fluorescently labeled POP-MNs-PDNV smoothly pierced the stratum corneum, and the trajectories, illustrated by the

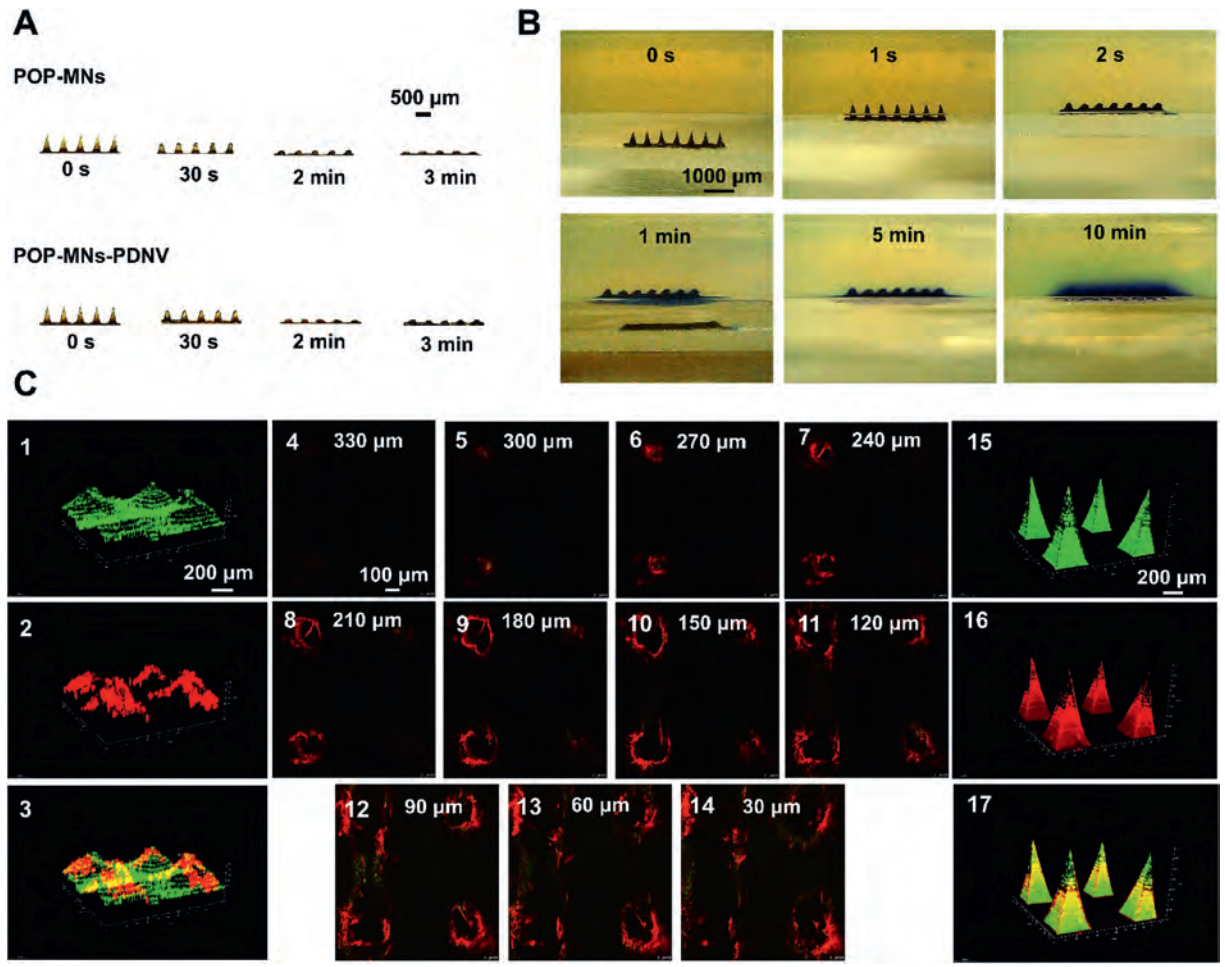

Figure 4 Characterization and performance of microneedles in skin puncture and drug delivery. (A) Solubility of the microneedles on *ex vivo* mouse skin. (B) Solubility of microneedles in artificial skin. (C) Fluorescence distribution of DiO-labeled PDNV (green) and RhB-labeled substrate (red) in microneedle-punctured skin (1−3 are 3D reconstructed images of POP-MNs-PDNV punctured skin, 4−14 are RhB fluorescence pictures of longitudinal sections of the skin punctured by and 15−17 are 3D reconstructed images of POP-MNs-PDNV).

fluorescence distribution, were similar between the depths of 0−120 μm, but pores became smaller along with the increase of the penetration depth between 120 and 330 μm, which was consistent with the shape of the microneedles (Fig. 4C). Due to the elastic deformation of the skin, the total puncture depth was understandably smaller than the microneedle length. In addition, the green fluorescent DiO-labeled PDNV were found to be uniformly distributed in the microneedles, which proved the accurate dosage of during PDNV delivery.

3.4. Enhanced transdermal penetration of PDNV by POP-MNs-PDNV

Fluorescence tracing of POP-MNs-PDNV with DiO-labeled PDNV and RhB-labeled substrates showed a significant increase in the amount and depth of PDNV penetration within 10 min to 1 h after *in vivo* transdermal administration, and a small amount of PDNV passed through the skin at 30 min (Fig. 5A). In contrast, DiO-labeled PDNV itself were mainly retained in the epidermis with the highest concentration in the stratum corneum, and only a small fraction was absorbed further into the skin *via* appendages (Fig. 5B), which indicated that the size of PDNV hindered their penetration into the skin[43]. Moreover, nanoparticle tracking analysis after Franz cell diffusion test using *ex vivo* mouse skin discs showed that (Fig. 5C), DiO-labeled PDNV were not found in the receiving solution at any of the time intervals examined, whereas a large number of nanoparticles penetrated the skin from 10 min, and the amount further increased at 30 min in the POP-MNs-PDNV group. But at 1 h time point, nanoparticle fluorescence intensity decreased most likely attributed to fluorescence quenching. No DiO-labeled PDNV was detected in the receiving solution of the PDNV group without microneedle assistance, which was consistent with the results of the *in vivo* transdermal assay, suggesting that it is difficult to maintain the intact morphology of PDNV through the skin after transdermal administration, and that the mechanism of its transdermal penetration may involve multiple pathways, including fusion with the stratum corneum, lipid exchange, and gradual release of the content, which may result in the structural alteration of the PDNV, and thus it cannot be detected by instrumentation in the form of nanoparticles.

In general, microneedling significantly improved the transdermal penetration efficiency and the distribution of PDNV in the skin, hence enhancing their topical anti-inflammatory properties.

3.5. PDNV and POP inhibit abnormal proliferation of HaCaT cells and promote M1-to-M2 phenotype transformation of RAW264.7 cells

POP concentrations in the range of 1−6 and 0.8−10 mg/mL were not cytotoxic to HaCaT cells (Fig. 6A) and RAW264.7 cells

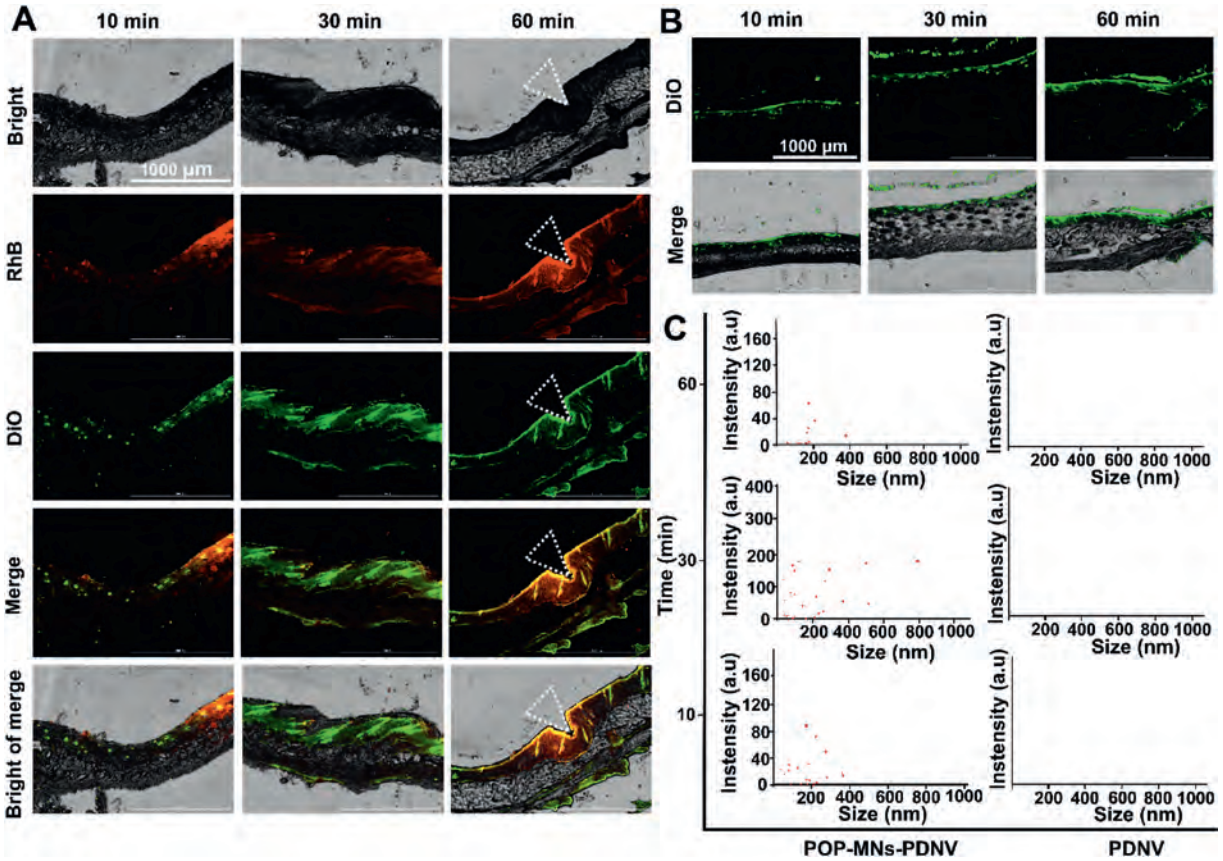

Figure 5 Transdermal delivery properties of POP-MNs-PDNV. (A) Fluorescence images of skin sections after *in vivo* transdermal administration of POP-MNs-PDNV with DiO-labeled PDNV (green) and RhB-labeled substrates (red). (B) Fluorescence pictures of skin sections after *in vivo* transdermal administration of an aqueous solution of PDNV labeled with DiO (green). (C) Nanoparticle tracking analysis of the receiving fluid in Franz cell diffusion test after *in vitro* transdermal administration of POP-MNs-PDNV prepared with DiO-labeled PDNV and RhB-labeled substrates versus an aqueous solution of DiO-labeled PDNV.

(Fig. 6B), respectively, and the PDNV protein concentrations in the range of 50−800 μg/mL were safe to both cells (Fig. 6C and D). Since PDNV are intact natural vesicles, the release and utilization of encapsulated polysaccharides, proteins, nucleic acids and other active substances highly depend on the efficient internalization of PDNV by target cells. PDNV were progressively absorbed by HaCaT cells and RAW264.7 cells and exclusively localized to the cytoplasm in a time-dependent manner. While the accumulation of nanovesicles peaked at 8 h of administration, fluorescence gradually weakened, suggesting the digestion of the intracellular PDNV (Fig. 6E).

TNF-α successfully induced significantly facilitated cell proliferation in HaCaT cells (Supporting Information Fig. S9), and while the administration of POP and PDNV alone, as well as the combination of the two, significantly inhibited this elevated level of cell multiplication (Fig. 7A−C), respectively. The most significant effects ($P < 0.0001$) were observed in 1 mg/mL POP (Figs. 7A), 100 μg/mL (protein concentration) of PDNV (Figs. 7B) and 0.05 mg/mL (protein concentration) PDNV+ 0.5 mg/mL POP (Fig. 7C). Additionally, remarkable release of inflammatory factor NO was triggered by LPS in RAW264.7 cells (Supporting Information Fig. S10), and was significantly reduced by the application of POP (0.5−10 mg/mL) (Fig. 7D), PDNV (protein concentration of 100−800 μg/mL) (Fig. 7E), and PDNV (protein concentration of 0.1 mg/mL) + POP (0.1−2 mg/mL) groups (Fig. 7F), respectively, with the 4 mg/mL POP and 600 μg/mL PDNV (Fig. 7E), and PDNV (protein concentration of 0.1 mg/mL) + POP (2 mg/mL) (Fig. 7F) had the most significant inhibitory effect ($P < 0.0001$).

The expression of TNF-α, which facilitates the mobilization and sensitization of inflammatory cells, and is also involved in modulating immune response and apoptotic processes[44], in RAW264.7 cells was significantly elevated by LPS stimulation ($P < 0.0001$, Fig. 7G). IL-6, another important inflammatory factor, was also upregulated in RAW264.7 cells by LPS stimulation ($P < 0.0001$, Fig. 7H). IL-6 is involved in the regulation of immune response, the promotion of B cell differentiation and proliferation, and plays a vital role in inflammation and tissue

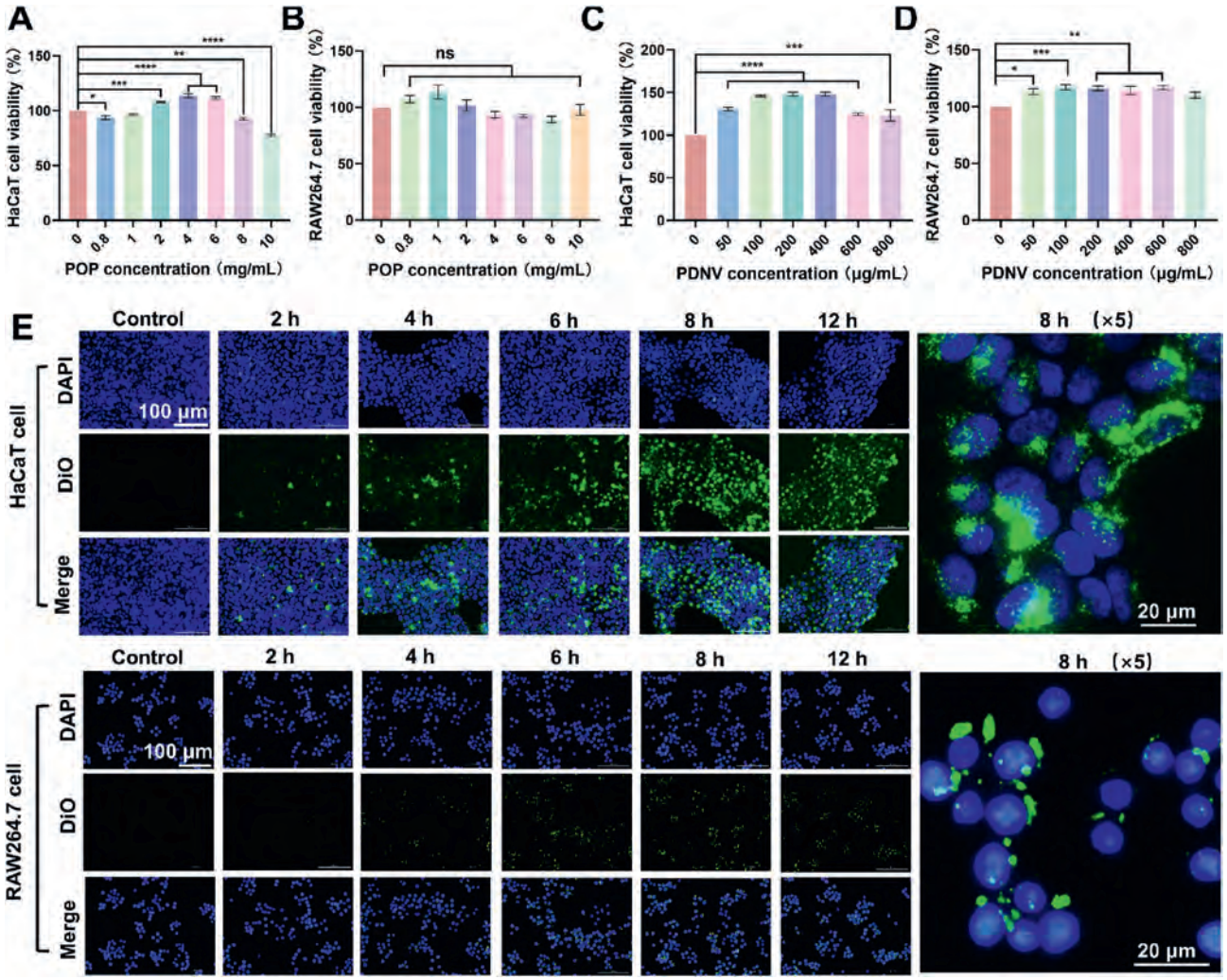

Figure 6 Interactions of PDNV and POP with HaCaT and RAW264.7 cells. (A, B) Cytotoxicity of POP and PDNV on HaCaT cells, respectively. (C, D) Cytotoxicity of POP and PDNV on RAW264.7 cells, respectively. (E) Immunofluorescent imaging of HaCaT and RAW264.7 cells demonstrating internalization of DiO-labeled PDNV. Data are expressed as mean ± SD (ns, non-significant, $*P < 0.05$, $**P < 0.01$, $***P < 0.001$, $****P < 0.0001$; $n = 4$).

repair[45]. Administration of PDNV, POP, or PDNV + POP significantly down-regulated TNF-α and IL-6 expression, and still the most prominent effect was observed in the PDNV + POP group (Fig. 7G and H).

We next investigated the influence of PDNV and POP on the polarization of RAW264.7 cells. The distinct polarization states of macrophages dictate their pivotal function in orchestrating inflammatory processes and preserving physiological equilibrium[46]. RAW264.7 cells were labeled with CD206, a receptor characteristic of M2-type macrophages, and CD86, a receptor characteristic of M1-type macrophages, respectively, and the numbers of macrophages of both phenotypes were measured[47,48]. LPS treatment polarized RAW264.7 cells to M1-type macrophages, and there was a noticeable shift of polarization towards M2-type after treatments (Fig. 7J). In addition, it was observed that, while normal macrophages were mostly spherically shaped, LPS treatment caused the cells to shift to a shuttle shape with long tentacles. PDNV, POP, as well as PDNV + POP treatments, were all able to reshape the LPS-induced cells to rounded and elliptical morphology (Supporting Information Fig. S11). Further analysis showed that, compared to PDNV or POP alone, PDNV + POP exhibited the most significant effect on raising the M2/M1 macrophage cell number ratio, suggesting a synergistic anti-inflammatory capability of the combination ($P < 0.0001$, Fig. 7I).

Studies have shown that a shift in macrophage polarization from M1 to M2 polarization is closely associated with the alleviation of inflammation[49]. M1-type macrophages are polarized by LPS and produce large amounts of pro-inflammatory factors such as TNF-α and IL-6[50]. This shift in polarization has been shown to be associated with the elevation of the inflammatory factors TNF-α, and IL-6 by the mechanism of inhibiting the activation of the NF-κB inflammatory pathway. The elevation of TNF-α and IL-6 is also present in the alteration of macrophage polarization induced by

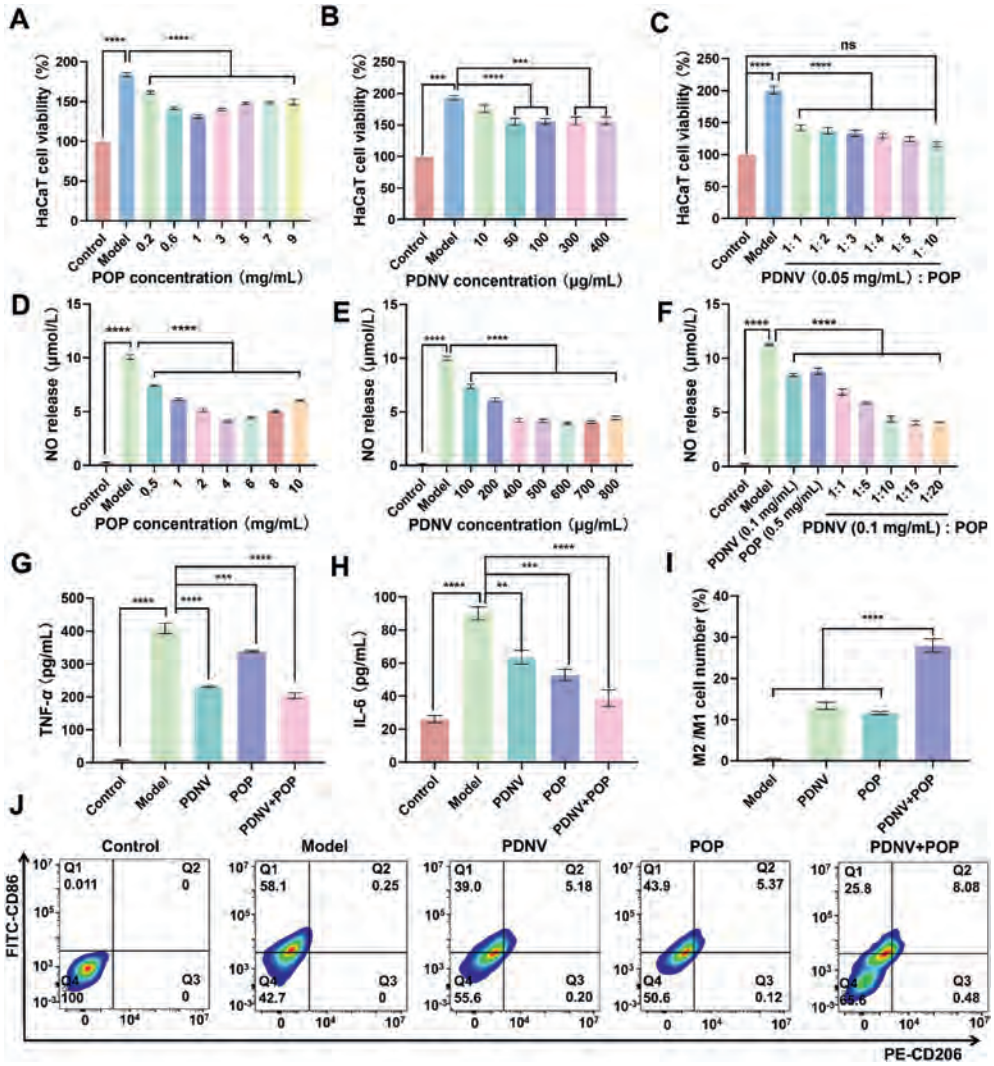

Figure 7 Effects of POP and PDNV on inflammatory cells. (A−C) Effects of POP, PDNV, and PDNV + POP on the 80 ng/mL TNF-α induced proliferation of HaCaT cells, respectively. (D−F) Effects of POP, PDNV, and PDNV + POP, on the 1 μg/mL LPS induced NO release from RAW264.7 cells, respectively. (G, H) Effect of each test group on TNF-α and IL-6 release from 1 μg/mL LPS-induced RAW264.7 cells, respectively. (I) Alteration of M2/M1 cell number ratio. (J) Flow cytometry diagrams of M1 and M2 phenotype RAW264.7 cells under various treatments. Data are expressed as mean ± SD (ns, non-significant, $^{**}P < 0.01$, $^{***}P < 0.001$, $^{****}P < 0.0001$, $n = 3$).

PDNV, and it is therefore very likely that PDNV also relieve atopic dermatitis by inhibiting the NF-κB inflammatory pathway.

3.6. POP and PDNV exert anti-inflammatory functions via regulating the gene expression of pro- and anti-inflammatory cytokines in RAW264.7 cells

Transcriptome sequencing followed by PCA analysis revealed that POP, PDNV and POP + PDNV treatments all markedly influence the gene expression profile of LPS-induced RAW264.7 cells (Supporting Information Fig. S12). As expected, LPS administration caused significant variation of expression in a large number of genes (Supporting Information Fig. S13A). However, it is noteworthy that the combination of POP and PDNV was able to modulate the expression of more genes compared to any of the treatments alone on these LPS-administered RAW264.7 cells, implying a cooperative effect of the two (Fig. S13B−S13D). The top 10 most significant differential genes selected from each treatment group were *Basp1*, *Slfn5*, *Slpi*, *Traf1*, *Cd80*, *Pgf*, *Pdgfb*, *Tnf*, *Ms4a6c* (Fig. S13B); *Cmpk2*, *Rsad2*, *Ifit2*, *Oasl2*, *Ifit3*, *Cxcl10*, *Ccrl2*, *lfih1*, *Gbp3*, *Rrm2* (Fig. S13C); and *Ccl5*, *Cmpk2*, *Rassf4*, *Rsad2*, *Ifit1*, *Ifit2*, *Ifit3*, *mt-Nd5*, *Cxcl3*, *Il6* (Fig. S13D). GO analysis showed that genes, which were significantly influenced by the treatments, were associated with immune response, cellular process and biological regulation (Fig. 8A), and POP + PDNV group was enriched with a higher number of immunomodulation-related genes, which was more significant. KEGG enrichment analysis was then employed and able to identify several immune pathways that were dramatically impacted, including the TNF signaling pathway, NOD-like receptor (NLR) signaling pathway, and NF-κB signaling pathway (Fig. 8B), with POP + PDNV group showing the biggest influence. The TNF signaling pathway involves the interaction of TNF and its receptor TNFR[51], which is associated with the regulation of cellular adhesion and metabolism, including inflammatory diseases, autoimmune diseases, and tumors[52]. The NOD-like receptor signaling pathway triggers immune and inflammatory responses by recognizing intracellular pathogen molecules or host-derived damage signals[53]. NF-κB regulates immune responses, inflammation, cell proliferation, and apoptosis[54]. Activation of

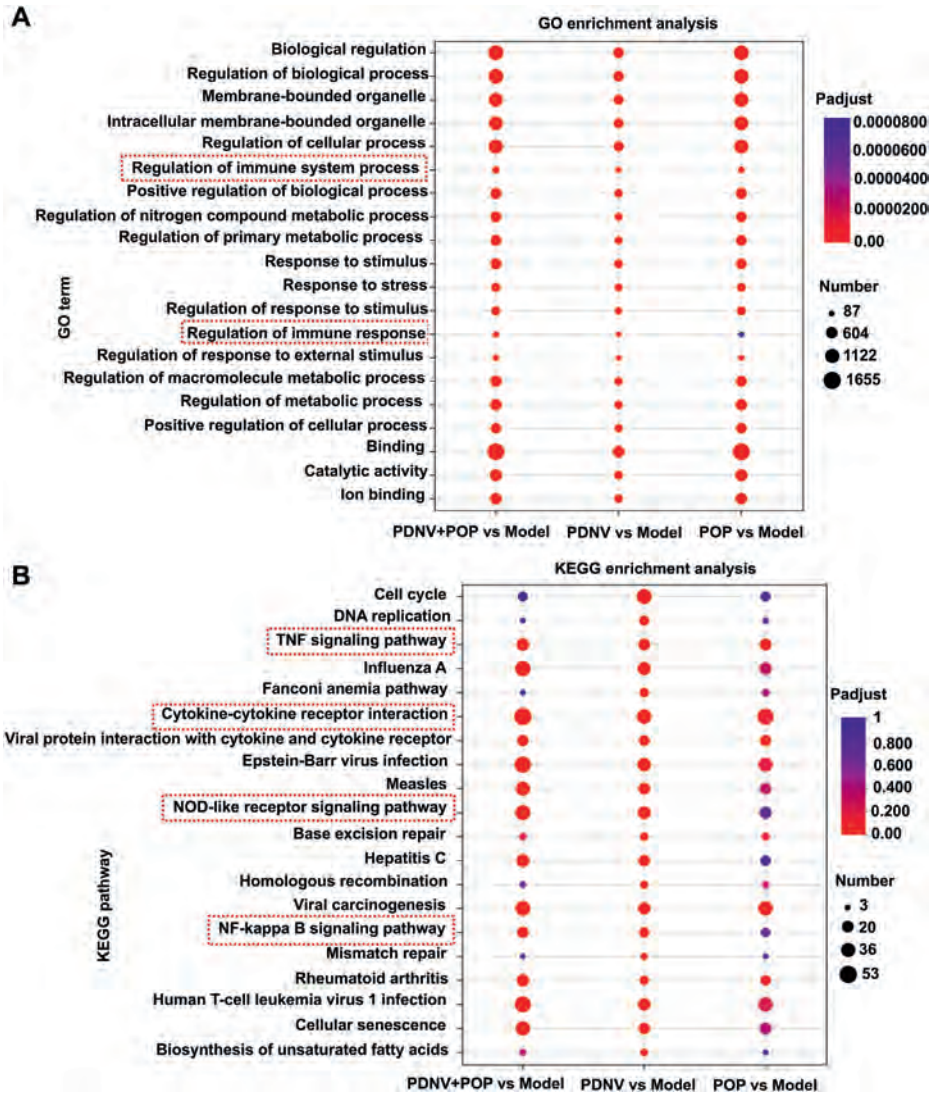

Figure 8 Transcriptomic analysis of PDNV and POP treated inflammatory RAW264.7 cells. (A, B) GO and KEGG enrichment analysis of differentiated genes, respectively. (Red dashed boxes represent screened immune-related annotations and signaling pathways).

NF-κB signaling *via* TNFR1 by TNF is essential to maintain tissue homeostasis and counter inflammation[55]. In addition, the activation of NLRs induces the formation of inflammatory vesicles in the NOD-like receptor signaling pathway, which in turn activates caspase-1 and promotes the maturation and secretion of IL-1β and IL-18, which are part of the NF-κB signaling pathway[56,57]. Our finding suggests that, while LPS induces macrophage polarization to M1 type and activates the NF-κB signaling pathway through TNF signaling pathway and NOD signaling pathway, leading to the secretion of large amounts of pro-inflammatory cytokines, whereas inhibition of pro-inflammatory cytokine, PDNV treatment exerts its anti-inflammatory effects, at least in part, *via* the inhibits the NF-κB signaling pathway.

The Model *vs.* Control and POP *vs.* Model groups were further screened for intersecting genes and a new gene set "POP" was created, and the same method was used to screen the gene set "PDNV" and the gene set "PDNV + POP". The three newly created gene sets were subjected to GO and KEGG enrichment analyses, and the results of GO enrichment analyses showed that there were more entries related to immune processes (Fig. 9A), and KEGG also enriched immune-related pathways, including TNF signaling pathway, cytokine interactions, IL-17 signaling pathway (Fig. 9B), and the number and significance of genes enriched in the PDNV + POP set was also stronger. The IL-17 signaling pathway is a signaling pathway mediated by IL-17 family cytokines, including IL-17A to IL-17F, which plays a key role in immune responses, especially in inflammatory responses and host defense[58].

Since from the analysis above it was clear that genes and pathways involved in immune response and regulation were significantly affected by the treatments, we then further focused on key individual candidates in order to uncover underlying

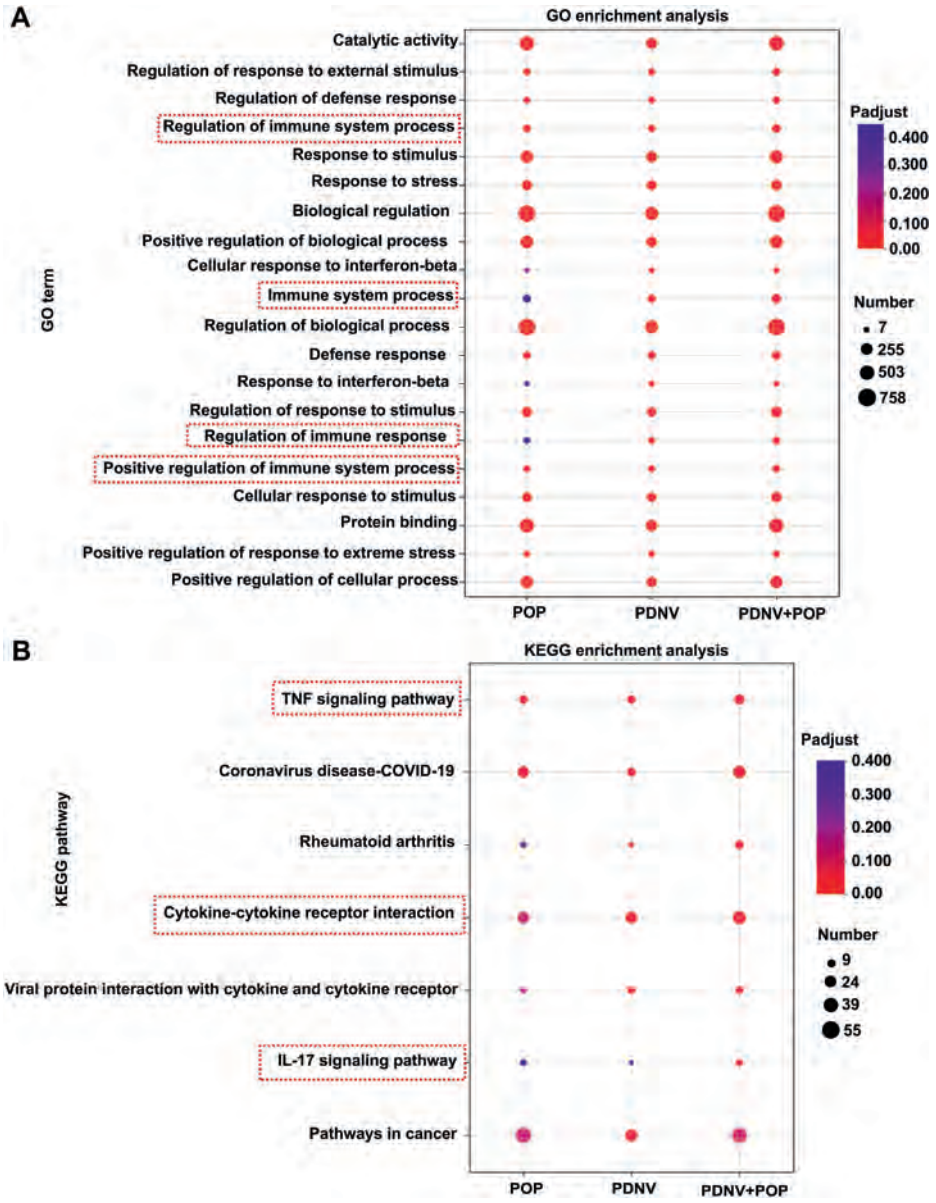

Figure 9 Functional enrichment analysis of immune-related differentially expressed genes *via* GO (A) and KEGG (B) enrichment analysis. (Red dashed boxes represent screened immune-related annotations and signaling pathways).

mechanisms by which PDNV and POP exhibit their anti-inflammatory effects. Multiple genes, including *TNF* (Fig. 10A), which is mainly produced by activated macrophages and regulates the proliferation and differentiation of immune cells[59], *IL-1β* (Fig. 10B), a pro-inflammatory cytokine[60], *IL-6* (Fig. 10C), which regulates immune and inflammatory responses[61], and chemokine (C−C motif) ligand 2 (*CCL2*), *CCL4*, and *CCL5* (Fig. 10D−F), which modulate the migration of immune cells by binding to specific chemokine receptors[62,63], were found to be abnormally elevated by LPS stimulation, but were significantly downregulated after the administration of treatments, among which the PDNV + POP group had the strongest effect. In summary, the combined treatment of POP and PDNV significantly improved the inflammatory status of LPS-induced RAW264.7 cells by modulating multiple immune-related genes and signaling pathways, showing synergistic anti-inflammatory effects.

3.7. POP-MNs-PDNV evidently alleviate DNCB-induced AD symptoms in mice

One week of DNCB administration in mice resulted in dryness, erythema, epidermal detachment, and thickening in the skin, whereas the positive control Dex was able to almost completely reverse the damage (Fig. 11A and B). Different levels of improvement were observed in other treatment groups, with POP-MNs-PDNV showing the most obvious effect (Fig. 11B and C). HE staining analysis showed that the epidermis of normal mice was smooth and had no sign of inflammatory infiltration, while the epidermis and dermis of the AD model group were greatly thickened and the dermis was severely infiltrated by inflammatory cells, which were effectively ameliorated by all treatment groups, among which POP-MNs-PDNV displayed the most significant effect (Fig. 11D and Supporting Information Fig. S14). It was further observed from toluidine blue stained skin sections that the model control group had the highest number of mast cells. In contrast, the number of mast cells decreased after drug administration (Fig. 11E and Supporting Information Fig. S15). Notably, the POP-MNs-PDNV group showed the most significant improvement, which was consistent with the results of HE staining analysis.

Skin barrier dysfunction is one of the major causes of AD. Skin water loss is accelerated, leading to dry, flaky skin and increased transdermal water loss from the skin. The therapeutic effect of POP-MNs-PDNV was investigated using a DNCB-induced mouse model of AD. The model group had the highest rate of transdermal water loss, which was effectively reduced with the use of Dex (Fig. 12A, $P < 0.0001$), and the skin barrier function was restored. POP-MNs-PDNV also reduced the rate of transdermal water loss and alleviated the damaged skin barrier function (Fig. 12A, $P < 0.01$).

We also noted that persistent stimulation with DNCB significantly elevated the spleen index, suggesting an impaired immune system (Fig. 12B, $P < 0.0001$, Supporting Information Fig. S16)[64]. Treatment with POP-MNs-PDNV, POP-MNs, and PDNV alone all markedly reduced the elevated spleen index (Fig. 12B, $P < 0.0001$, Fig. S16), implying that they have an effect on normalizing the immune function. In addition, IgE is considered one of the major indicators of allergic reactions *in vivo*, and AD is typically characterized by high serum IgE, while total IgE levels are strongly correlated with the severity of the disease[65]. DNCB-induced serum IgE levels were significantly higher in mice than in normal mice, but improved after two weeks of administration of POP-MNs-PDNV and POP-MNs (Fig. 12C).

We then explore the influence of PDNV and microneedles on the expression of immune-related cytokines in AD model mice *in vivo*. TNF-α is a major proinflammatory cytokine that participates in intrinsic and adaptive immune responses by regulating immune cell differentiation and inflammatory factor production,

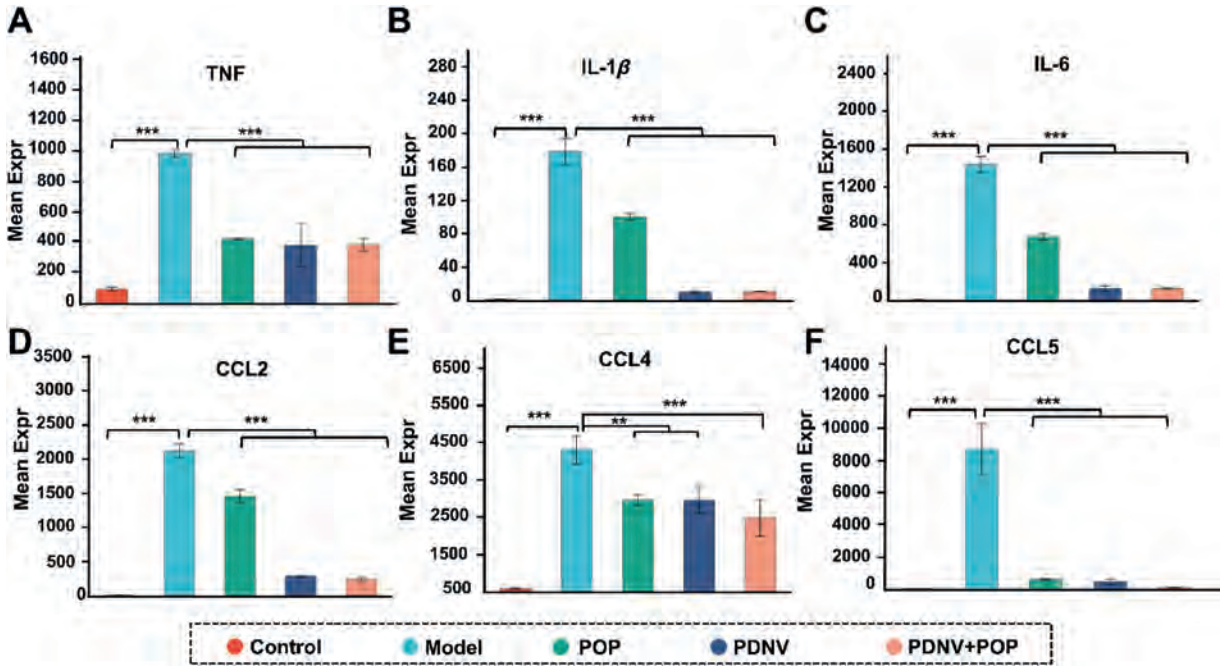

Figure 10 Gene expression analysis of *TNF* (A), *IL-1β* (B), *IL-6* (C), *CCL2* (D), *CCL4* (E), and *CCL5* (F) in PDNV and POP treated inflammatory RAW264.7 cells. Data are expressed as mean ± SD (**$P < 0.01$, ***$P < 0.001$, $n = 3$).

and IL-4 is a key Th2 cytokine that drives IgE-mediated allergic inflammation in AD[66,67]. Whereas INF-γ, which is produced by Th1 cells, plays an important role in regulating immune responses and inhibiting Th2-type responses[68]. DNCB induction caused significant elevation of the expression of TNF-α (Fig. 12D, $P < 0.0001$) and IL-4 (Fig. 12E, $P < 0.0001$), as well as significant reduction of INF-γ level (Fig. 12F, $P < 0.001$), in the skin tissue, as detected by ELISA. While, as predicted, Dex significantly decreased TNF-α (Fig. 12D, $P < 0.001$) and IL-4 release (Fig. 12E, $P < 0.0001$), and also markedly raised INF-γ concentration (Fig. 12F, $P < 0.01$), it was rather exciting to discover that POP-MNs-PDNV exhibited significantly improving effects comparable to the glucocorticoid (TNF-α: Fig. 12D, $P < 0.01$; IL-4: Fig. 12E, $P < 0.0001$; INF-γ: Fig. 12F, $P < 0.01$). In comparison, POP-MNs and PDNV were relatively less effective, indicating a dramatic synergistic activity of the two. The above findings were verified by RT-PCR analysis, which showed that POP-MNs-PDNV significantly decreased mRNA expression of *Tnf-α* (Fig. 12G, $P < 0.0001$) and *Il-4* (Fig. 12H, $P < 0.05$), while increasing mRNA expression of *Ifn-γ* (Fig. 12I, $P < 0.05$).

POP-MNs-PDNV had significant effects in regulating immune responses and reducing inflammation by decreasing the levels of TNF-α and IL-4 while up-regulating the expression of INF-γ. POP-MNs-PDNV were able to effectively inhibit the Th2-type response and enhance the Th1-type response, thereby attenuating DNCB-induced AD. The anti-inflammatory effects were possibly exerted through multiple mechanisms, including direct inhibition of inflammatory cell activation, regulation of cytokine secretion, and promotion of immune cell homeostasis.

To determine whether the NF-κB signaling pathway, which has previously been shown to be inhibited by PDNV in macrophages (Fig. 8B), mediates the anti-inflammatory effects of our therapies *in vivo*, we examined the expression patterns of NF-κB p65 and its phosphorylated form (p-NF-κB p65) in skin tissues. NF-κB p65 and p-NF-κB p65 are two key components of the NF-κB signaling pathway and can reflect its activation status[69]. When activated,

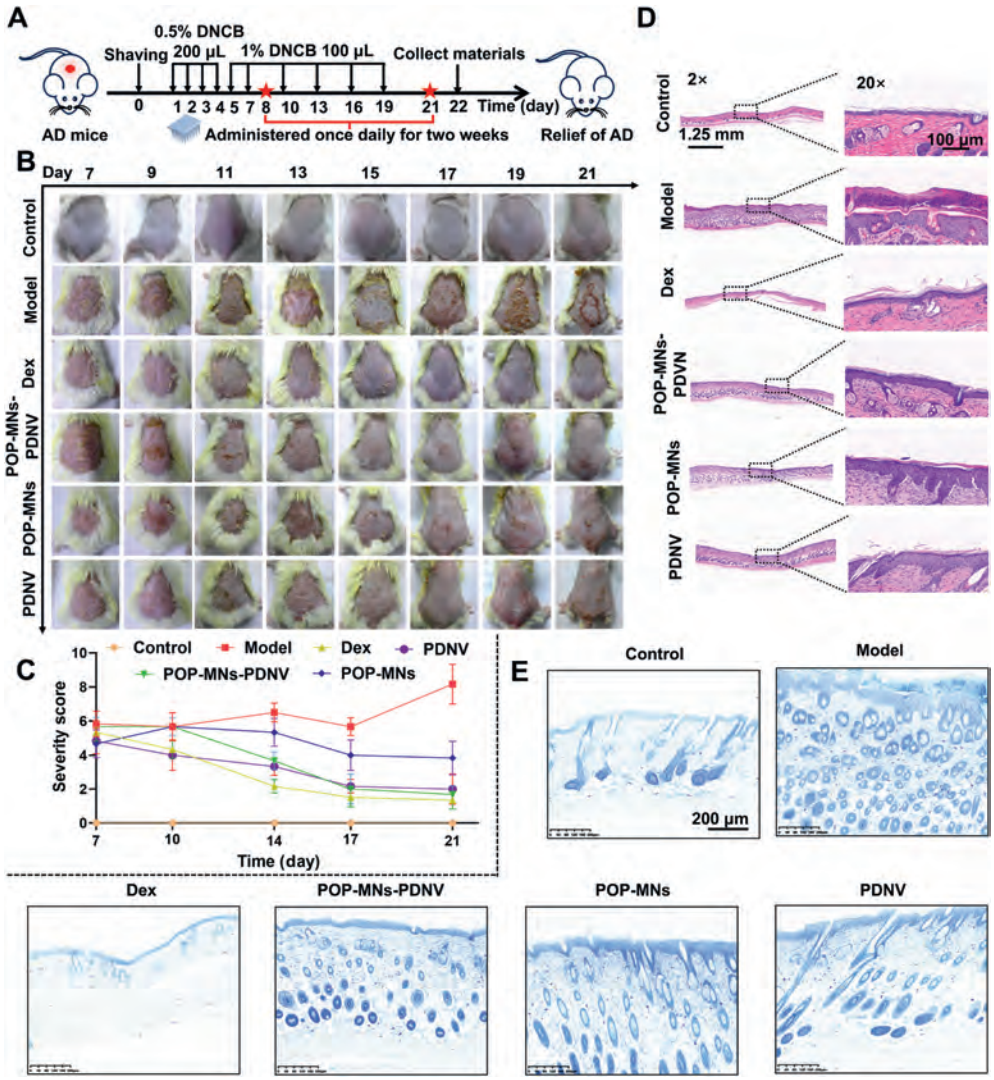

Figure 11 Symptomatic improvement by POP-MNs-PDNV in mouse AD model. (A) Flowchart of *in vivo* pharmacodynamics experiments. (B) Photographic observation of the dorsal skin of mice under different treatment conditions. (C) EASI score alteration by various treatments over time. (D, E) H&E staining and toluidine blue staining of the skin sections, respectively.

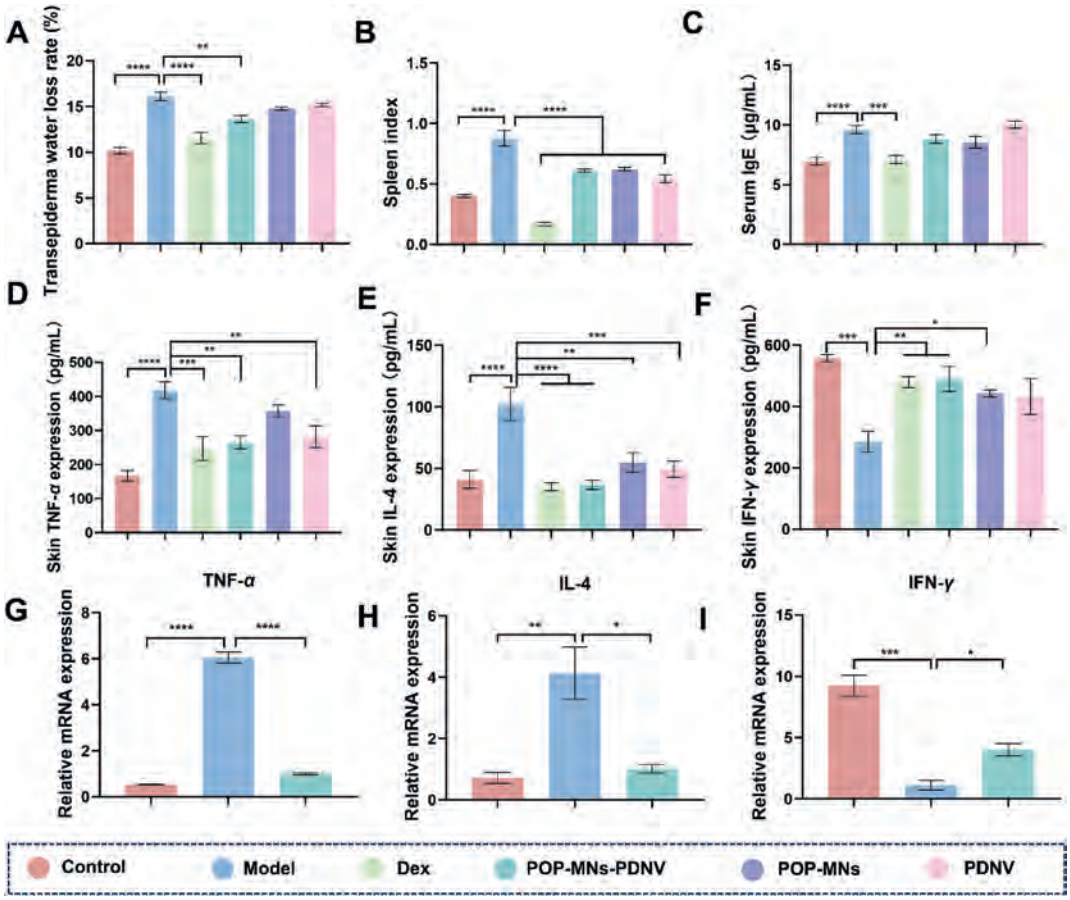

Figure 12 Effects of POP-MNs-PDNV treatment on skin barrier function and immune response in AD model mouse. (A) Transdermal water loss rate ($n = 3$). (B) The spleen index. (C) Serum IgE. (D−F) TNF-α, IL-4, and IFN-γ expression in the skin, respectively. (G−I) mRNA expression of *Tnf-α*, *Il-4*, and *Ifn-γ*, respectively ($n = 3$). Data are expressed as mean ± SD (*$P < 0.05$, **$P < 0.01$, ***$P < 0.001$, ****$P < 0.0001$, $n = 6$).

they directly increase the expression of a variety of inflammatory factors such as TNF-α, IL-4, and IL-6, which are crucial in inflammatory response and immune regulation[55]. IHC analysis showed that both NF-κB p65 and p-NF-κB p65 were significantly upregulated in the DNCB-induced mice compared with the normal control group (Fig. 13A), suggesting that the NF-κB pathway was over-activated. Notably, POP-MNs-PDNV treatment reduced its expression to a level comparable to that of the potent anti-inflammatory reference Dex, whereas POP-MNs or PDNV alone showed only a partial inhibitory effect (Fig. 13A). WB assays further confirmed that the p-NF-κB p65/NF-κB p65 ratio was significantly elevated in the model control group, whereas PDNV effectively normalized it (Fig. 13B and C), which highlighted the excellent performance of POP-MNs-PDNV in inhibiting the NF-κB pathway.

We went on to analyze another important protein, STING, which is involved in the regulation of cellular immune responses to pathogens and cellular stress[70], and has been recently reported to regulate the onset and progression of a number of skin diseases, like AD and psoriasis[71]. In the model control group, DNCB strongly induced STING protein expression, and POP-MNs-PDNV treatment virtually eliminated this challenge, consistent with the effect of Dex (Fig. 13A). In contrast, POP-MNs or PDNV treatment alone had a weaker inhibitory effect on STING (Fig. 13A), highlighting the synergistic effect between POP and PDNV. WB analysis confirmed these findings, showing that STING protein levels were significantly reduced in all treatment groups, with the most pronounced effect being shown with POP-MNs-PDNV (Fig. 13D). Collectively, these results suggest that POP-MNs-PDNV ameliorates AD through dual inhibition of the aberrant activation of the NF-κB and STING signaling pathways, with efficacy comparable to glucocorticoid therapy, while at the same time exerting a synergistic effect of the natural components.

The level of CD86 expression in the skin was significantly increased in the model group, indicating an intense inflammatory response, whereas it was decreased in all of the administered groups. Meanwhile, CD206 expression levels were significantly higher in the administered groups, and the lowest CD86 expression levels were found in the POP-MNs-PDNV, except for the positive drug group, suggesting that the POP-MNs-PDNV may promote the shift of macrophages from pro-inflammatory M1 type to anti-inflammatory and reparative-functioning M2 type, which contributes to the repair process of skin damage and the resolution of inflammation (Fig. 13E and F). The results are consistent with what was observed on LPS-induced macrophages when PDNV were applied (Fig. 7I and J), confirming the capability of modulating immune cell polarization by PDNV.

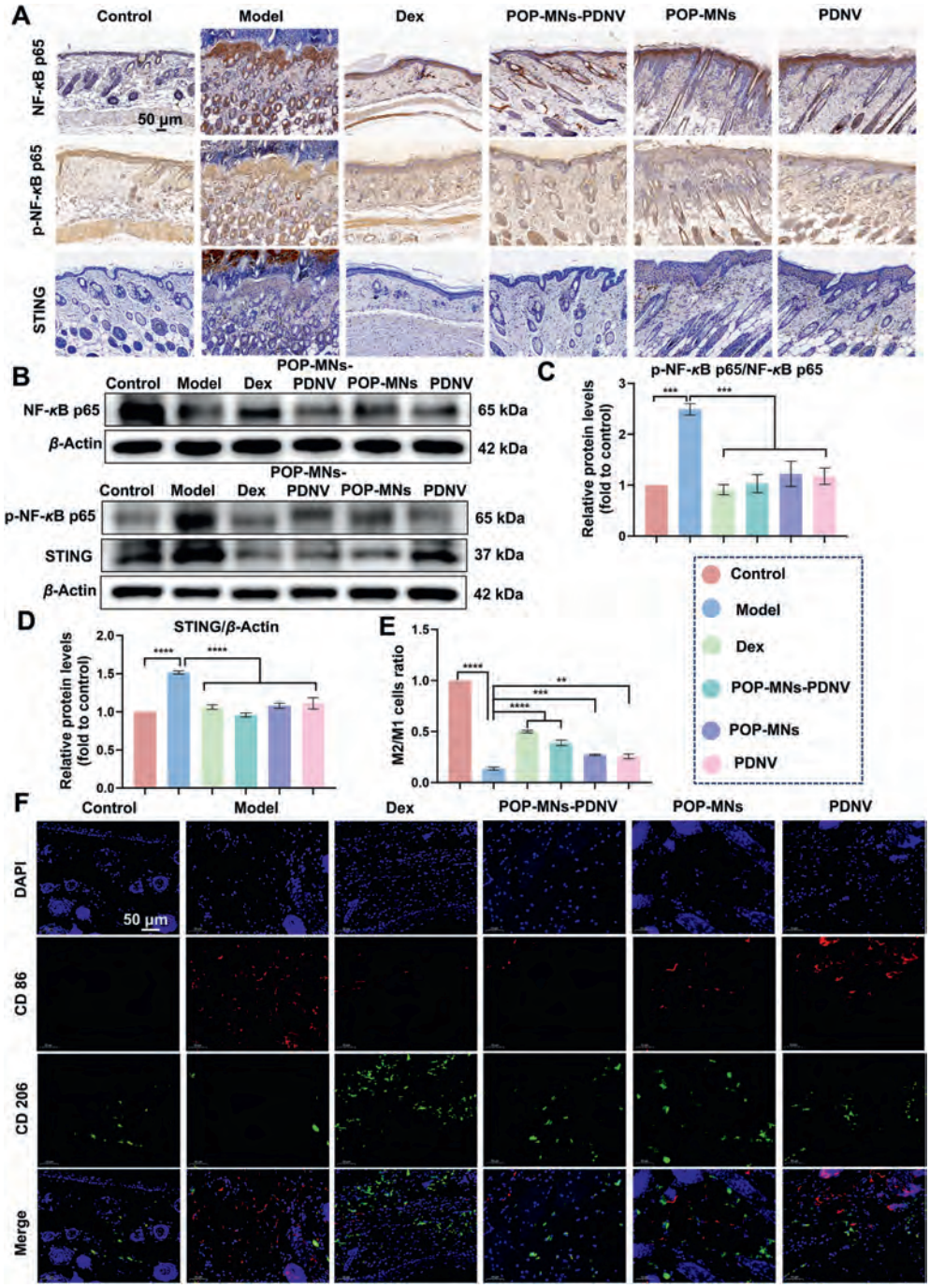

Figure 13 Potential immunomodulatory mechanisms of POP-MNs-PDNV to ameliorate AD symptoms in mice. (A) Immunohistochemical pictures of NF-κB p65, p-NF-κB p65, and STING protein expression in the skin under different treatments. (B) Western blot bands. (C, D) Statistical analysis of the expression of p-NF-κB p65/NF-κB p65 and STING in skin tissues, respectively. (E) Immunofluorescence quantification of CD206 (M2) and CD86 (M1). (F) Immunofluorescence images of CD86 and CD206 expression in the skin. Data are expressed as mean ± SD (**$P < 0.01$, ***$P < 0.001$, ****$P < 0.0001$, $n = 3$).

Taken together, we conclude that, although topical application of PDNV is effective, to some degree, against DNCB-induced AD in mice, a synergistic combination by the integration of the nanovesicles and polysaccharides into microneedles significantly enhanced their potency. This novel microneedle-assisted percutaneous preparation exhibited comparable effectiveness of ameliorating AD symptoms to glucocorticoid, potentially through the inhibition of the activation of the NF-κB and STING signaling pathways, and accompanied by a dramatic change of macrophage phenotype from M1 to M2.

3.8. Preliminary evaluation of biosafety of POP-MNs-PDNV

After the *in vivo* efficacy experiments, compared to the normal group, there were no significant changes in the heart, liver, spleen, lung, and kidney tissues in all treatment groups, except for the Dex

group, indicating the biosafety of POP-MNs-PDNV and their components. In contrast, long-term topical application of Dex affected the immune function, as evidenced by spleen atrophy and reduction of lymphocytes (Fig. 14A). More notably, Dex was found to significantly elevate the serum levels of hepatic function markers ALT (Fig. 14B, $P < 0.0001$), AST (Fig. 14C, $P < 0.001$), TP (Fig. 14E, $P < 0.0001$), but not TBIL (Fig. 14D), as well as important renal function indicators CR (Fig. 14F, $P < 0.05$) and UR (Fig. 14G, $P < 0.001$), suggesting its potential hepatorenal toxicity[72]. On the contrary, no significant alteration of any of the markers was detected in the POP-MNs-PDNV group, indicating its reassuring biosafety.

To further evaluate the cutaneous biocompatibility of POP-MNs-PDNV, the microneedles were first punctured into the shaved skin on the back of mice for 1 min before removal. The remaining barely noticeable impressions only lasted for about 5 min, and

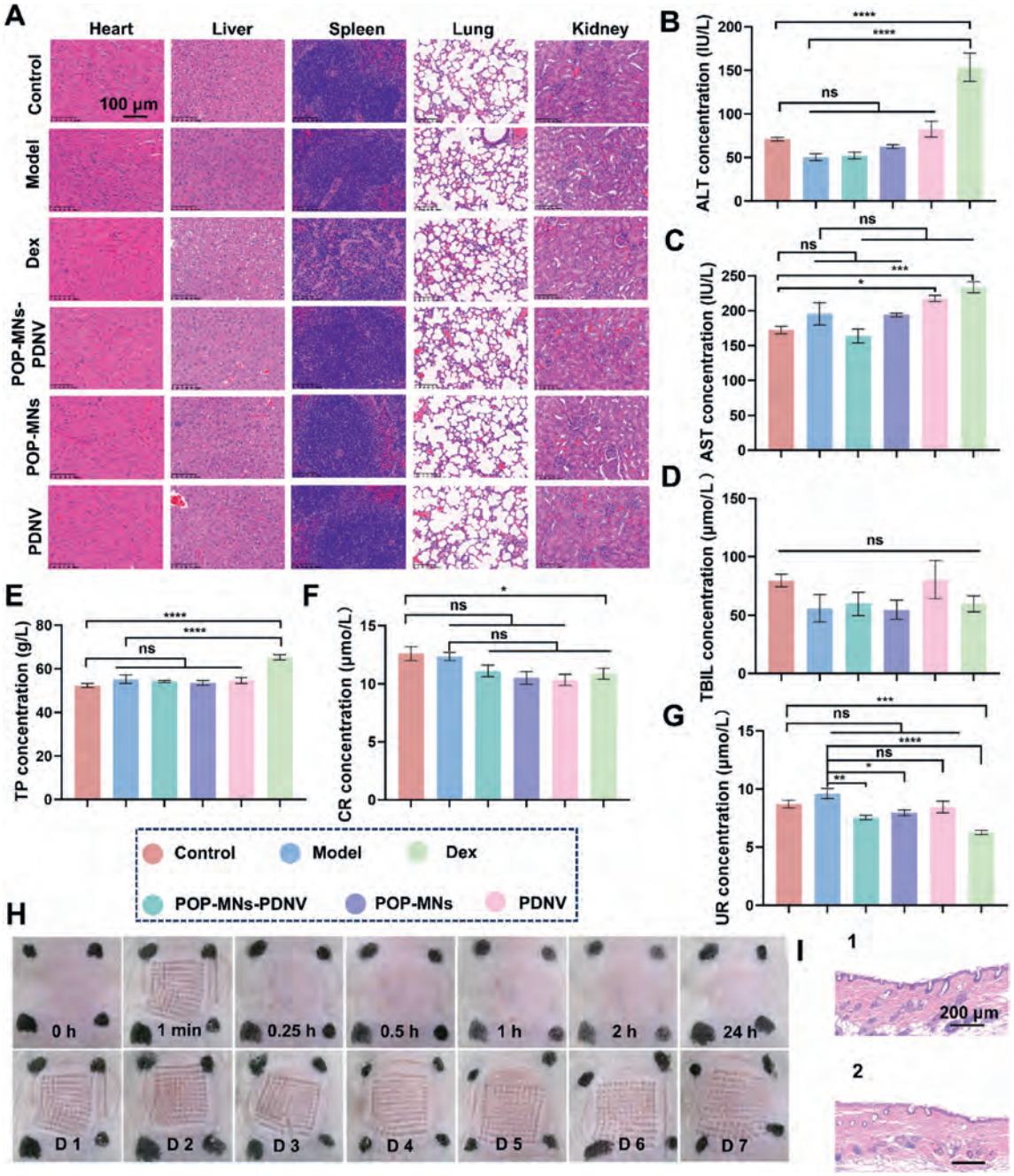

Figure 14 Biosafety evaluation of POP-MNs-PDNV. (A) Images of H&E-stained sections of the vital organs of mice after treatments. (B), (C), (D), (E), (F), and (G) Expression of ALT, AST, TBIL, TP, CR, and UR in the mice serum after the drug efficacy test, respectively. Data are expressed as mean ± SD (ns, non-significant; $*P < 0.05$, $**P < 0.01$, $***P < 0.001$, $****P < 0.0001$; $n = 6$). (H) Continuous observation of the mice skin surface after transient (1 min, top row) and long-term (once daily for 7 consecutive days, bottom row) administration of POP-MNs-PDNV. (I) Micrographs of H&E-stained mice skin sections after administration of POP-MNs-PDNV for 7 consecutive days (1, POP-MNs-PDNV group; 2, normal group).

then faded out by 2 h, while skin irritations, such as edema and erythema, also completely disappeared in 24 h (Fig. 14H). In addition, when POP-MNs-PDNV were applied repeatedly at the same site of the skin every day for 7 consecutive days, no obvious superficial damage or histological injury was observed in the skin tissue (Fig. 14H and I).

In summary, these data indicate that long-term usage of POP-MNs-PDNV on the skin would not cause any serious skin or systemic damage, thus demonstrating their biocompatibility and medicinal application potential.

4. Conclusions

As a very widely distributed, fast-growing and easily cultivated herb in the world, the development of *Portulaca oleracea* L. as a pharmaceutical raw material holds great economic and social benefits. The current work identified the potential of nanovesicles derived from *Portulaca oleracea* L. in treating AD, which was synergistically enhanced by polysaccharides from the same plant. More importantly, the efficacy of the nanovesicles was further significantly improved by using a dissolvable microneedle preparation which integrated HA and POP with PDNV. Underlying mechanisms of this novel treatment method involved the inhibition of NF-κB and STING pathways, and the M1-to-M2 transformation of macrophages. Our work provides a paradigm for the comprehensive exploitation of plant-derived nanovesicles, and also an advantageous and feasible therapeutic option against AD.

Acknowledgments

We thank the staff members of the Large-scale Protein Preparation System at the National Facility for Protein Science in Shanghai (NFPS), Shanghai Advanced Research Institute, Chinese Academy of Science, China for providing technical support and assistance in data collection and analysis, Prof. Luan Xin, Institute of Cross-Science, Shanghai University of Traditional Chinese Medicine, for providing Nanosight device testing services, Dr. Zongguang Tai of Shanghai Dermatology Hospital affiliated with Tongji University for providing the skin water loss rate test, and Shanghai Meiji Bio (https://www.majorbio.com/) for the transcriptome sequencing service. This work was supported by the National Natural Science Foundation of China (No. 82474197), the Program for Professor of Special Appointment (Eastern Scholar) at Shanghai Institutions of Higher Learning (No. TP2020054, China), Shanghai Seventh People's Hospital Medical Institution Preparation and Innovative Chinese Medicine R&D (Open Bidding for Selecting the Best Candidates) Project (No. QYCXZY250204, China), and the Program for Shanghai High-Level Local University Innovation Team (No. SZY20220315, China).

Author contributions

Meng Long: methodology, formal analysis, writing - original draft. Jiaqi Li: methodology, writing - original draft, visualization. Yuecheng Zhu: methodology, validation. Hang Ruan: validation. Jing Li: formal analysis. Fanjun Xu: formal analysis. Ruipeng Liu: formal analysis. Tao Yang: validation, resources, data curation, project administration. Yanqin Shi: methodology, validation, investigation, writing - review & editing, project administration, funding acquisition. Nianping Feng: validation, resources, project administration. Yongtai Zhang: conceptualization, methodology, validation, investigation, resources, writing - review & editing, supervision, project administration, funding acquisition.

Conflicts of interest

The authors declare no conflicts of interest.

Appendix A. Supporting information

Supporting information to this article can be found online at https://doi.org/10.1016/j.apsb.2025.08.021.

References

1. Langan SM, Irvine AD, Weidinger S. Atopic dermatitis. *Lancet* 2020; **396**:345−60.
2. Li HG, Zhang Z, Zhang H, Guo YF, Yao ZR. Update on the pathogenesis and therapy of atopic dermatitis. *Clin Rev Allergy Immunol* 2021;**61**:324−38.
3. Borok J, Matiz C, Goldenberg A, Jacob SE. Contact dermatitis in atopic dermatitis children-past, present, and future. *Clin Rev Allergy Immunol* 2019;**56**:86−98.
4. Passos MdCF, Moraes-Filho JP. Intestinal microbiota in digestive diseases. *Arq Gastroenterol* 2017;**54**:255−62.
5. Kleinman E, Laborada J, Metterle L, Eichenfield LF. What's new in topicals for atopic dermatitis?. *Am J Clin Dermatol* 2022;**23**:595−603.
6. Yang D, Chen ML, Sun Y, Jin YP, Lu C, Pan X, et al. Microneedle-mediated transdermal drug delivery for treating diverse skin diseases. *Acta Biomater* 2021;**121**:119−33.
7. Kim RW, Lam M, Abuabara K, Simpson EL, Drucker AM. Targeted systemic therapies for adults with atopic dermatitis: selecting from biologics and JAK inhibitors. *Am J Clin Dermatol* 2024;**25**:179−93.
8. Jin Z, Na JT, Lin X, Jiao R, Liu XY, Huang Y. Plant-derived exosome-like nanovesicles: a novel nanotool for disease therapy. *Heliyon* 2024; **10**:e30630.
9. Urzì O, Gasparro R, Ganji NR, Alessandro R, Raimondo S. Plant-RNA in extracellular vesicles: the secret of cross-kingdom communication. *Membranes* 2022;**12**:352.
10. Lian MQ, Chng WH, Liang J, Yeo HQ, Lee CK, Belaid M, et al. Plant-derived extracellular vesicles: recent advancements and current challenges on their use for biomedical applications. *J Extracell Vesicles* 2022;**11**:e12283.
11. Wu JQ, Ma XY, Lu Y, Zhang T, Du ZQ, Xu J, et al. Edible *Pueraria lobata*-derived exosomes promote M2 macrophage polarization. *Molecules* 2022;**27**:8184.
12. Bian YP, Li WZ, Jiang XQ, Yin F, Yin L, Zhang YL, et al. Garlic-derived exosomes carrying miR-396e shapes macrophage metabolic reprograming to mitigate the inflammatory response in obese adipose tissue. *J Nutr Biochem* 2023;**113**:109249.
13. Trentini M, Zanolla I, Zanotti F, Tiengo E, Licastro D, Dal Monego S, et al. Apple derived exosomes improve collagen type I production and decrease MMPs during aging of the skin through downregulation of the NF-κB pathway as mode of action. *Cells* 2022;**11**:3950.
14. Huang RF, Jia B, Su DD, Li MC, Xu ZX, He C, et al. Plant exosomes fused with engineered mesenchymal stem cell-derived nanovesicles for synergistic therapy of autoimmune skin disorders. *J Extracell Vesicles* 2023;**12**:e12361.
15. Lv WJ, Huang JY, Li SP, Gong XP, Sun JB, Mao W, et al. *Portulaca oleracea* L. extracts alleviate 2,4-dinitrochlorobenzene-induced atopic dermatitis in mice. *Front Nutr* 2022;**9**:986943.
16. Wang YJ, Viennet C, Jeudy A, Fanian F, He L, Humbert P. Assessment of the efficacy of a new complex antisensitive skin cream. *J Cosmet Dermatol* 2018;**17**:1101−7.
17. Zhu MZ, Xu HM, Liang YJ, Xu J, Yue NN, Zhang Y, et al. Edible exosome-like nanoparticles from *portulaca oleracea* L mitigate DSS-

induced colitis *via* facilitating double-positive $CD4^+CD8^+$ T cells expansion. *J Nanobiotechnol* 2023;**21**:309.
18. López de Las Hazas M-C, Tomé-Carneiro J, Del Pozo-Acebo L, Del Saz-Lara A, Chapado LA, Balaguer L, et al. Therapeutic potential of plant-derived extracellular vesicles as nanocarriers for exogenous miRNAs. *Pharmacol Res* 2023;**198**:106999.
19. Waghule T, Singhvi G, Dubey SK, Pandey MM, Gupta G, Singh M, et al. Microneedles: a smart approach and increasing potential for transdermal drug delivery system. *Biomed Pharmacother* 2019;**109**: 1249−58.
20. Wan T, Pan Q, Ping Y. Microneedle-assisted genome editing: a transdermal strategy of targeting NLRP3 by CRISPR-Cas9 for synergistic therapy of inflammatory skin disorders. *Sci Adv* 2021;**7**: eabe2888.
21. Wen WL, Yang J, Liang X, Li YL, Zhang WY, Sun X, et al. Construction of cryomicroneedles loaded with milk-derived exosomes encapsulated TNF-α siRNA and efficacy of percutaneous acupoint administration in rheumatoid arthritis. *Int J Pharm* 2024;**657**:124159.
22. Bui VD, Son S, Xavier W, Nguyen VQ, Jung JM, Lee J, et al. Dissolving microneedles for long-term storage and transdermal delivery of extracellular vesicles. *Biomaterials* 2022;**287**:121644.
23. Saha I, Rai VK. Hyaluronic acid based microneedle array: recent applications in drug delivery and cosmetology. *Carbohydr Polym* 2021;**267**:118168.
24. Hou XL, Long M, Feng NP, Zhang YT. Natural food-derived materials fabricated nanocapsules-dissolving microneedles system for treating primary dysmenorrhea. *Food Hydrocoll* 2023;**144**:12.
25. Du HY, Liu P, Zhu JJ, Lan JJ, Li Y, Zhang LB, et al. Hyaluronic acid-based dissolving microneedle patch loaded with methotrexate for improved treatment of psoriasis. *ACS Appl Mater Interfaces* 2019;**11**: 43588−98.
26. Wu T, Hou XL, Li JQ, Ruan H, Pei LX, Guo T, et al. Microneedle-mediated biomimetic cyclodextrin metal organic frameworks for active targeting and treatment of hypertrophic scars. *ACS Nano* 2021; **15**:20087−104.
27. Ruan H, Long M, Li JQ, Zhang D, Feng NP, Zhang YT. Sustained-release hydrogen-powered bilateral microneedles integrating CD-MOFs for *in situ* treating allergic rhinitis. *Adv Healthcare Mater* 2024;**13**:e2400637.
28. Zhou P, Zhao SY, Huang C, Qu Y, Zhang C. *Bletilla striata* polysaccharide microneedle for effective transdermal administration of model protein antigen. *Int J Biol Macromol* 2022;**205**:511−9.
29. Wang M, Li CJ, Li JY, Hu WJ, Yu AQ, Tang HP, et al. Extraction, purification, structural characteristics, biological activity and application of polysaccharides from *Portulaca oleracea* L. (Purslane): a review. *Molecules* 2023;**28**:4813.
30. Chen QB, Li Q, Liang YQ, Zu MH, Chen NX, Canup BSB, et al. Natural exosome-like nanovesicles from edible tea flowers suppress metastatic breast cancer *via* ROS generation and microbiota modulation. *Acta Pharm Sin B* 2022;**12**:907−23.
31. Iqbal J, Khan AA, Aziz T, Ali W, Ahmad S, Rahman SU, et al. Phytochemical investigation, antioxidant properties and *in vivo* evaluation of the toxic effects of *Parthenium hysterophorus*. *Molecules* 2022;**27**:4189.
32. Xu N, Gao YP, Li Z, Chen Y, Liu ML, Jia JZ, et al. Immunoregulatory hydrogel decorated with Tannic acid/Ferric ion accelerates diabetic wound healing *via* regulating Macrophage polarization. *Chem Eng J* 2023;**466**:143173.
33. Chen MJ, Li D, Meng XW, Sun Y, Liu R, Sun TD. Review of isolation, purification, structural characteristics and bioactivities of polysaccharides from *Portulaca oleracea* L. *Int J Biol Macromol* 2024; **257**:128565.
34. Xia L, Deji Zhu M, Chen D, Lu Y. *Juniperus pingii var.* wilsonii acidic polysaccharide: extraction, characterization and anticomplement activity. *Carbohydr Polym* 2020;**231**:115728.
35. Li WJ, Luo FL, Wu XH, Fan B, Yang MR, Zhong W, et al. Anti-inflammatory effects and mechanisms of dandelion in RAW264.7 macrophages and zebrafish larvae. *Front Pharmacol* 2022;**13**:906927.
36. Riedl R, Kühn A, Rietz D, Hebecker B, Glowalla KG, Peltner LK, et al. Establishment and characterization of mild atopic dermatitis in the DNCB-induced mouse model. *Int J Mol Sci* 2023;**24**:12325.
37. Koskeridis F, Evangelou E, Ntzani EE, Kostikas K, Tsabouri S. Treatment with dupilumab in patients with atopic dermatitis: systematic review and meta-analysis. *J Cutan Med Surg* 2022;**26**: 613−21.
38. Liu XM, Yan JY, Wu XP, Wu X, Zhang YJ, Li B. Biosafety evaluation of $Li_2Si_2O_5$whisker-reinforced glass-ceramics. *Biomed Mater* 2022; **17**:025011.
39. Asl ER, Amini M, Najafi S, Mansoori B, Mokhtarzadeh A, Mohammadi A, et al. Interplay between MAPK/ERK signaling pathway and MicroRNAs: a crucial mechanism regulating cancer cell metabolism and tumor progression. *Life Sci* 2021;**278**:119499.
40. Li YX, Ren MJ, Yan H, Luo L, Fang X, He L, et al. Purification, structural characterization, and immunomodulatory activity of two polysaccharides from Portulaca oleracea L. *Int J Biol Macromol* 2024; **264**:130508.
41. Chen XF, Yue ZL, Winberg PC, Dinoro JN, Hayes P, Beirne S, et al. Development of rhamnose-rich hydrogels based on sulfated xylorhamno-uronic acid toward wound healing applications. *Biomater Sci* 2019;**7**:3497−509.
42. Burton SA, Ng CY, Simmers R, Moeckly C, Brandwein D, Gilbert T, et al. Rapid intradermal delivery of liquid formulations using a hollow microstructured array. *Pharm Res* 2011;**28**:31−40.
43. Xiang H, Xu S, Li JY, Pan SH, Miao XQ. Particle size effect of curcumin nanocrystals on transdermal and transfollicular penetration by hyaluronic acid-dissolving microneedle delivery. *Pharmaceuticals* 2022;**15**:206.
44. Tu YM, Gong CX, Ding L, Liu XZ, Li T, Hu FF, et al. A high concentration of fatty acids induces TNF-α as well as NO release mediated by the P2X4 receptor, and the protective effects of puerarin in RAW264.7 cells. *Food Funct* 2017;**8**:4336−46.
45. Yang GP, Gu MH, Chen WS, Liu WH, Xiao YB, Wang HX, et al. SPHK-2 promotes the particle-induced inflammation of RAW264.7 by maintaining consistent expression of TNF-α and IL-6. *Inflammation* 2018;**41**:1498−507.
46. Wang SX, Cao M, Xu SH, Shi JF, Mao XD, Yao XM, et al. Luteolin alters macrophage polarization to inhibit inflammation. *Inflammation* 2020;**43**:95−108.
47. Ren SJ, Zhou R, Tang ZS, Song ZX, Li N, Shi XB, et al. Wuling capsule modulates macrophage polarization by inhibiting the TLR4−NF-κB signaling pathway to relieve liver fibrosis. *Int Immunopharmacol* 2024;**129**:111598.
48. Song JY, Zeng J, Zheng SL, Jiang N, Wu AG, Guo SM, et al. *Sanguisorba officinalis* L. promotes diabetic wound healing in rats through inflammation response mediated by macrophage. *Phytother Res* 2023;**37**:4265−81.
49. Hu ZJ, Chen D, Yan PH, Zheng F, Zhu HY, Yuan ZW, et al. Puerarin suppresses macrophage M1 polarization to alleviate renal inflammatory injury through antagonizing TLR4/MyD88-mediated NF-κB p65 and JNK/FoxO1 activation. *Phytomedicine* 2024;**132**:155813.
50. Sun J, Liao Z, Li ZY, Li H, Wu ZM, Chen C, et al. Down-regulation miR-146a-5p in Schwann cell-derived exosomes induced macrophage M1 polarization by impairing the inhibition on TRAF6/NF-κB pathway after peripheral nerve injury. *Exp Neurol* 2023;**362**: 114295.
51. Alam MS, Otsuka S, Wong N, Abbasi A, Gaida MM, Fan Y, et al. TNF plays a crucial role in inflammation by signaling *via* T cell TNFR2. *Proc Natl Acad Sci U S A* 2021;**118**:e2109972118.
52. Kalliolias GD, Ivashkiv LB. TNF biology, pathogenic mechanisms and emerging therapeutic strategies. *Nat Rev Rheumatol* 2016;**12**: 49−62.
53. Almeida-da-Silva CLC, Savio LEB, Coutinho-Silva R, Ojcius DM. The role of NOD-like receptors in innate immunity. *Front Immunol* 2023;**14**:1122586.
54. Sun SC. The non-canonical NF-κB pathway in immunity and inflammation. *Nat Rev Immunol* 2017;**17**:545−58.

55. Hayden MS, Ghosh S. Regulation of NF-κB by TNF family cytokines. *Semin Immunol* 2014;**26**:253−66.
56. Van Quickelberghe E, De Sutter D, van Loo G, Eyckerman S, Gevaert K. A protein−protein interaction map of the TNF-induced NF-κB signal transduction pathway. *Sci Data* 2018;**5**:180289.
57. Wertz IE. TNFR1-activated NF-κB signal transduction: regulation by the ubiquitin/proteasome system. *Curr Opin Chem Biol* 2014;**23**:71−7.
58. Li X, Bechara R, Zhao J, McGeachy MJ, Gaffen SL. IL-17 receptor-based signaling and implications for disease. *Nat Immunol* 2019;**20**: 1594−602.
59. Balkwill F. Tumour necrosis factor and cancer. *Nat Rev Cancer* 2009; **9**:361−71.
60. Gabay C, Lamacchia C, Palmer G. IL-1 pathways in inflammation and human diseases. *Nat Rev Rheumatol* 2010;**6**:232−41.
61. Rose-John S, Jenkins BJ, Garbers C, Moll JM, Scheller J. Targeting IL-6 trans-signalling: past, present and future prospects. *Nat Rev Immunol* 2023;**23**:666−81.
62. Chen YY, Liu SY, Wu LL, Liu YT, Du J, Luo ZH, et al. Epigenetic regulation of chemokine (CC-motif) ligand 2 in inflammatory diseases. *Cell Prolif* 2023;**56**:e13428.
63. Patterson SJ, Pesenacker AM, Wang AY, Gillies J, Mojibian M, Morishita K, et al. T regulatory cell chemokine production mediates pathogenic T cell attraction and suppression. *J Clin Investig* 2016;**126**: 1039−51.
64. Viallard JF, Parrens M, Blanco P, Moreau JF, Oksenhendler E, Fieschi C. Influence of splenomegaly and splenectomy on the immune cell profile of patients with common variable immunodeficiency disease. *J Clin Immunol* 2024;**44**:46.
65. Czarnowicki T, He H, Krueger JG, Guttman-Yassky E. Atopic dermatitis endotypes and implications for targeted therapeutics. *J Allergy Clin Immunol* 2019;**143**:1−11.
66. Zelová H, Hošek J. TNF-α signalling and inflammation: interactions between old acquaintances. *Inflamm Res* 2013;**62**:641−51.
67. Yamanishi Y, Mogi K, Takahashi K, Miyake K, Yoshikawa S, Karasuyama H. Skin-infiltrating basophils promote atopic dermatitis-like inflammation *via* IL-4 production in mice. *Allergy* 2020;**75**: 2613−22.
68. Fagundes BO, de-Sousa TR, Victor JR. Gamma-delta ($\gamma\delta$) T cell-derived cytokines (IL-4, IL-17, IFN-γ and IL-10) and their possible implications for atopic dermatitis development. *Int J Dermatol* 2023; **62**:443−8.
69. Tang J, Xu LQ, Zeng YW, Gong F. Effect of gut microbiota on LPS-induced acute lung injury by regulating the TLR4/NF-κB signaling pathway. *Int Immunopharmacol* 2021;**91**:107272.
70. Zhang X, Bai XC, Chen ZJ. Structures and mechanisms in the cGAS−STING innate immunity pathway. *Immunity* 2020;**53**:43−53.
71. Huang C, Li WT, Ren XY, Tang MD, Zhang KY, Zhuo F, et al. The crucial roles and research advances of cGAS−STING pathway in cutaneous disorders. *Inflammation* 2023;**46**:1161−76.
72. Xie HG, Wang SK, Cao CC, Harpur E. Qualified kidney biomarkers and their potential significance in drug safety evaluation and prediction. *Pharmacol Ther* 2013;**137**:100−7.